

Analysis of Ultra-relativistic Charged Particle Beam
and Stretched Wire Measurement Interactions
with Cylindrically Symmetric Structures

by

C. E. Deibele

A dissertation submitted in partial fulfillment
of the requirements for the degree of

Doctor of Philosophy
(Electrical Engineering)

at the

UNIVERSITY OF WISCONSIN - MADISON

1996

Table of Contents

Abstract	v
Acknowledgments	vi
I. Overview.	1
A. Introduction.	1
B. Definitions	3
C. General Coupling Theory	9
D. Review of Past Work	11
E. Goals	21
II. Specific Source Considerations.	23
A. Introduction.	23
B. Ultra-relativistic Point Charge	23
C. Impulse of Current on a Center Conductor.	24
D. Ultra-relativistic Gaussian Bunch	25
E. Ultra-relativistic Time-Limited-Cosine-Squared.	26
F. Summary	28
III. Determination of a New Integral Equation.	30
A. Background Definitions.	30
B. Derivation of Equation.	30
IV. Charged Particle Beam Solution.	36
A. Theoretical Solution to the Integral Equation	36
B. Considerations for Calculating the Beam Impedance	40

i.	Choosing the Dimension to the Linear Equation40
ii.	Choosing the Frequencies and Number of Frequency Points.41
iii.	Perfect Conducting Boundary Considerations.42
C.	Computational Results45
i.	Assumptions45
ii.	Perfect Conducting Boundary Modification.46
iii.	Comparison of Theory to Measurement48
D.	Conclusions51
V.	Stretched Wire Analysis52
A.	Theoretical Solution.52
i.	Introduction.52
ii.	Change in Pipe Kernel Definition and Cavity Coupling.52
iii.	Addition of a Loss Mechanism and Data Modification.55
iv.	Change in Definition of the Beam Impedance.56
v.	Beampipe Cutoff Frequency Change.57
vi.	Example of a Relationship between SWM to Beam Impedance60
a.	Introduction60
b.	Calculation of Z_{beam}61
c.	Calculation of S_{21}63
vii.	Summary65
B.	Center Conductor Cutoff Effects66
C.	Measurement Data.69
i.	Introduction.69

ii.	Network Analyzer Measurement Considerations70
a.	Reference Measurement.70
b.	Pillbox Cavity Measurement and Prediction. . .	.74
iii.	Time Domain Measurements and Results.76
iv.	Comparison of Beam Impedance to Circuit Impedance83
a.	Introduction83
b.	50- Ω Reference Line Measurement of Circuit Impedance83
c.	Use of Non-50- Ω Reference Lines85
D.	Conclusion.89
VI.	Summary and Conclusions.91
Appendix A.	Derivation of Relationship Between Beam Impedance and Wakefield.96
Appendix B.	Fourier Transform Definitions and Conventions.	99
Appendix C.	Fourier Transform Property	100
Appendix D.	Beampipe and Cavity Matrix Computations. . .	101
A.	Primary Integration Result.	101
B.	Explicit Formulae for the Pipe and Cavity Matrices.	101
C.	Truncation Error Analysis	104
Appendix E.	Derivation of Circuit Parameters from S_{21} Measurements	109
A.	Introduction.	109
B.	Background Theory	109
C.	Application of Background Theory to SWM	111
Appendix F.	Bibliography	113

Abstract

*Analysis of Ultra-relativistic Charged Particle Beam
and Stretched Wire Measurement Interactions
with Cylindrically Symmetric Structures*

C. E. Deibele

Under the supervision of Professor J. Beyer

At the University of Wisconsin-Madison

The beam impedance and wakefield are quantities which describe the stability of charged particles in their trajectory within an accelerator. The stretched wire measurement technique is a method which estimates the beam impedance and wakefield. Definitions for the beam impedance, the wakefield, and the stretched wire measurement are presented. A pillbox resonator with circular beampipes is studied for its relatively simple profile and mode structure. Theoretical predictions and measurement data are presented for the interaction of various charged particle beams and center conductor geometries between the cavity and beampipe. Time domain predictions for the stretched wire measurement and wakefield are presented and are shown to be a linear interaction.

Acknowledgments

I wish to sincerely thank Professor Beyer, Dr. Robert Kustom, and the Advanced Photon Source (APS) at Argonne National Laboratory for their generous help and support for my research. They have helped me grow professionally, personally, and academically.

I also wish to thank the entire rf group from the APS. Tim Jonasson and Leonard Morrison were invaluable for their technical expertise. I am grateful to the many patient discussions with Dr. Yoon Kang and Dr. Ali Nassiri. I wish to thank Bill Berg and Chuck Gold of the diagnostics group at the APS for helping me with network analyzer dilemmas. I thank Dr. Joshua Song for his help with time domain measurements. I am also grateful for my frequent discussions with Jian Zhou.

Much of this work relied upon measurements and interpretations by the High Energy Physics (HEP) group at Argonne National Laboratory. Their help in both the understanding and interpretation of wakefields was essential. Additionally, I want to thank Professor Gluckstern at the University of Maryland for his comments regarding his past work.

I am grateful to the patience of Wolfgang Sturhahn, Sarvjit Shastri, and the rf group (including Dr. Kang, Dr.

Nassiri, and Geoff Waldschmidt) for their generous allowance and sharing of computer CPU time. I am also indebted to Tim Berenc and Joe Midlock for their computer expertise in both FORTRAN programming and Unix tutorials.

I am very grateful for the support and understanding of my friends. Erik Kemps has been a close companion who has been both a fixture and synonym of strength for me. Fred Ingram and Edith Zareba have made my tenure in Chicago a most welcome and wonderful time. The times we spent together certainly will always be both significant and memorable.

Finally and most importantly, I want to thank my mother for her continued support and confidence in me.

I. Overview

A. *Introduction*

Understanding the interaction of an ultra-relativistic particle bunch with its environment is crucial for designing a stable accelerator. Several articles have been written which describe this interaction in detail. Moreover, other papers have been written which describe a method whereby one may simulate this ultra-relativistic particle beam with a stretched wire. The goals of this dissertation are: 1) to lay some groundwork for a method for both solving and understanding the interaction of a charged particle beam with its environment, and 2) to compare the solutions of earlier papers which analyzed the stretched wire measurement (SWM) with theoretical solutions.

The results of the research are presented by first defining the wakefield, a particular problem faced by high energy scientists. An overview of the methods employed to solve particular wakefield phenomena will then be demonstrated, followed by the discussion of a new general integral equation which solves the wakefield problem. This integral equation governs the behavior of a particular geometry for both a high-energy charged particle beam and a wire simulation of the particle beam with its environment. A simple Fourier series technique is introduced which is shown to solve the integral equation, and the theoretical result is

compared to physical measurements. Finally, a comparison of results between a high-energy charged particle beam and a stretched wire measurement with a $50\text{-}\Omega$ coupling transmission line is presented.

The particle accelerator has become a tool for many disciplines of the sciences. As the study of particle accelerators grows, the understanding of the complex phenomena in the machine grows as well. A major limitation in the modern accelerator is the maximum level of current at which the machine can operate. Increasing the current in the machine typically raises the overall output of the machine. This is evident in high-energy accelerators where raising the current levels results in increasing the rate of collisions. In low-energy machines raising the current is helpful since scientific output is often proportional to current.

The accelerator often has practical limitations on the level of current it can reach because of inherent instability of the particles in their trajectory along the beampipe. Instabilities include disruptive forces from the interactions of the beam with its environment. The focus of many researchers has been to describe a way to predict the interactions of the particle bunch with its environment. This is accomplished with data from wakefield and beam impedance measurements.

The terms wakefield and beam impedance are sometimes

used interchangeably since the wakefield is the inverse Fourier transform of the beam impedance. Both of these quantities are used in dynamic equations for predicting beam stability. The formal derivation of the beam impedance from the wakefield is shown in Appendix A.

Many techniques are used to estimate the beam impedance. One technique which is commonly used is called the stretched wire measurement. The stretched wire measurement uses electromagnetic energy guided on a wire to simulate the fields from a relativistic beam of charges. Other techniques exist which measure the wakefield directly. Each measurement technique uses several approximations and therefore is prone to error when the measurement is not interpreted correctly.

B. Definitions

A physical description of the wakefield and beam impedance will be presented first, immediately followed by a mathematical description of these quantities. Before this can be accomplished however, the notion of voltage must be presented for a cavity resonator.

Figure 1-1 shows a profile of a simple beampipe structure. A section of beampipe leads into a simple pillbox resonator which

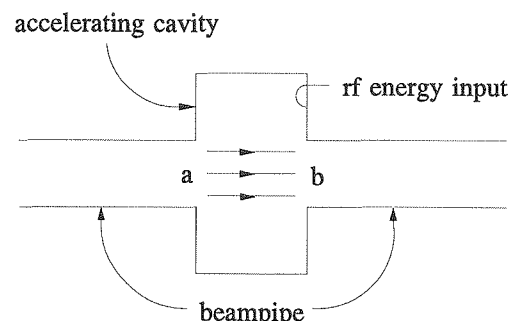


Figure 1-1. Coupling loop excites modes of the cavity with azimuthal electric field.

leads into another section of beampipe. The pillbox resonator has a coupling loop which is oriented to excite transverse magnetic (TM) modes of the resonator and thus produce an azimuthal electric field. The points a and b lie on the front and back walls of the resonator and are positioned on the beam trajectory which is along the center line of the resonator. With this geometry, the coupling loop in Fig. 1-1 has the capability to supply energy to the beam. This is easily seen using the simple force and energy relations in Eq. 1-1:

$$\begin{aligned}\vec{F} &= Q\vec{E} \\ \therefore \Delta E &= (Energy)|_{z=b} - (Energy)|_{z=a} \\ &= \int_a^b \vec{F} \cdot d\vec{l} = \int_a^b Q\vec{E} \cdot d\vec{z}.\end{aligned}\tag{1-1}$$

The accelerating voltage is defined by Eq. 1-2:

$$V_{accelerate} = \int_a^b \vec{E} \cdot \vec{z} \, dz.\tag{1-2}$$

Note that the accelerating voltage is a time harmonic quantity, and it is directly proportional to the energy gain of a charge as it passes through the cavity along the center of the beampipe.

The wakefield is a quantity easily described pictorially. In each of the following figures, the geometry

is the same as Fig. 1-1 without the rf input.

Envisage a point charge moving along the beampipe where it encounters a discontinuity similar to Fig. 1-2. The lines of electric field are shown to be extending outward radially as is predicted. As the charge progresses to the right in Fig. 1-3, it couples energy into the cavity and the boundary conditions of the cavity dictate a field picture as shown. These fields can exist in the cavity long after the particle leaves the resonator if the charge couples energy into a high Q mode of the cavity.

Figure 1-4 illustrates a

charge coupled to a high Q mode of the cavity, and either the

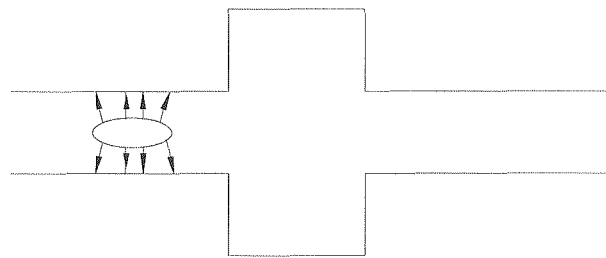


Figure 1-2. A point charge moving to the right before encountering beam pipe discontinuity.

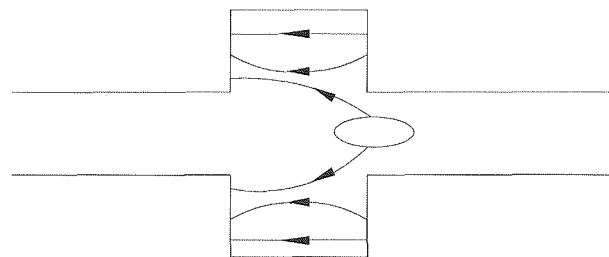


Figure 1-3. The point charge encounters the discontinuity and couples energy into the cavity.

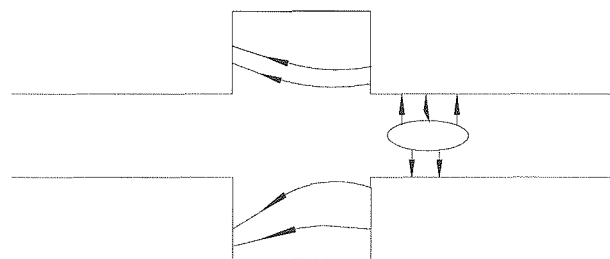


Figure 1-4. The point charge coupled energy into a high Q mode of the cavity leaving a wakefield along the beam's trajectory.

wall losses or the coupled propagating beampipe modes have not yet dissipated the energy supplied by the beam. This instantaneous field caused by a point charge is called the wakefield of the cavity. If another charge enters a cavity excited with a significant wakefield from an earlier charge or charges, the wakefield could make the latter charge trajectory become unstable and cause it to be lost to the machine. The wakefield shares the same properties as the accelerating voltage defined in Eq. 1-2 except the source of the accelerating voltage is typically considered to be the rf input while the source of the wakefield is a moving bunched charge.

The wakefield appears to be a rather abstract quantity but is easily defined with the help of some introductory linear system theory.

Envision a system,

described in Fig. 1-5,

whose input signal is $x(t)$

and whose impulse response

is $g(t)$. The function $g(t)$

represents a linear time invariant (LTI) system and therefore

$y(t)$ is easily predicted by Eq. 1-3, a convolution integral:

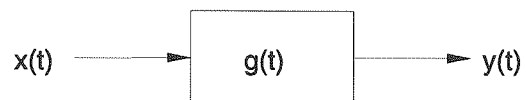


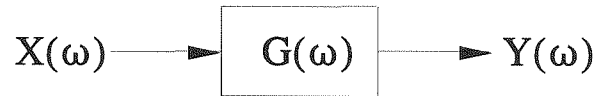
Figure 1-5. A linear time invariant (LTI) system.

$$y(t) = \int_{-\infty}^{+\infty} x(\tau) g(t-\tau) d\tau. \quad (1-3)$$

Note also that if $x(t)$ is the Dirac impulse function, $\delta(t)$, $y(t)$ is then simply the impulse response $g(t)$.

Inspection of Eq. 1-3 shows that if $g(t)$ is a complicated function, $y(t)$ could be computationally difficult to predict. Taking the Fourier transform of Eq. 1-3 would change the problem into studying the frequency domain response of the system. Typically speaking, the Fourier transform can simplify some integral and differential equations which govern system behavior and give another perspective in solving for the response of a system.

Figure 1-6 is the same system as in Fig. 1-5



except that each signal in

Figure 1-6. The Fourier-transformed system of Fig. 1-5.

Fig. 1-6 is the Fourier transform of the signal in Fig. 1-5. The function $Y(\omega)$ is easily computed since it is not defined by a convolution, as depicted in Eq. 1-3, but simply defined by multiplication as shown in Eq. 1-4:

$$Y(\omega) = X(\omega) G(\omega) . \quad (1-4)$$

A thorough description of these quantities can be found in many introductory linear system theory texts [1]. $G(\omega)$ will be defined as the beam impedance if $X(\omega)$ and $Y(\omega)$ have the proper definitions which follow.

The connection to beam impedance lies in applying a few definitions. Define $y(t)$ to be the wakefield voltage of an

arbitrary current source:

$$y(t) \triangleq \int_a^b \vec{E} \cdot \vec{z} dz,$$

where \vec{E} is the instantaneous electric field from a charge passing through an arbitrary structure. Consistent with the definitions in Fig. 1-5, define $x(t)$ to be the current in the machine which causes the wakefield $y(t)$:

$$x(t) \triangleq i(t),$$

where $x(t)$ is an impulse of current. The system response $y(t)$ is easily predicted with the convolution integral for this particular source. The result is summarized below:

$$y(t) = \int_{-\infty}^{\infty} g(t-\tau) x(\tau) d\tau = \int_{-\infty}^{\infty} g(t-\tau) \delta(\tau) d\tau = g(t).$$

This equation illustrates the wakefield voltage is the impulse response to the system in Fig. 1-3. Measuring the wakefield voltage from an impulse of current yields $g(t)$, the impulse response. From linear system theory, the behavior of the impulse response $g(t)$ uniquely determines the wakefield voltage for any excitation current $x(t)$.

Now consider the Fourier-transformed quantities

$$\begin{aligned} Y(\omega) &= \mathcal{F}\{y(t)\} \\ X(\omega) &= \mathcal{F}\{x(t)\} \\ G(\omega) &= \mathcal{F}\{g(t)\} \end{aligned}$$

Using the same definitions for each quantity presented earlier, it is clear from Eq. 1-2 that the SI unit of $G(\omega)$ is the ohm, and $G(\omega)$ is an impedance-type quantity which determines the response of any steady state current distribution. $G(\omega)$ is defined to be the beam impedance, and $Y(\omega)$ is defined to be the beam voltage.

C. General Coupling Theory

A general model [2] for coupling into a cavity is depicted in Fig. 1-7. The ideal turns ratio, a function of frequency, is a unique term for each mode and describes the level of coupling to individual cavity modes. The inductors

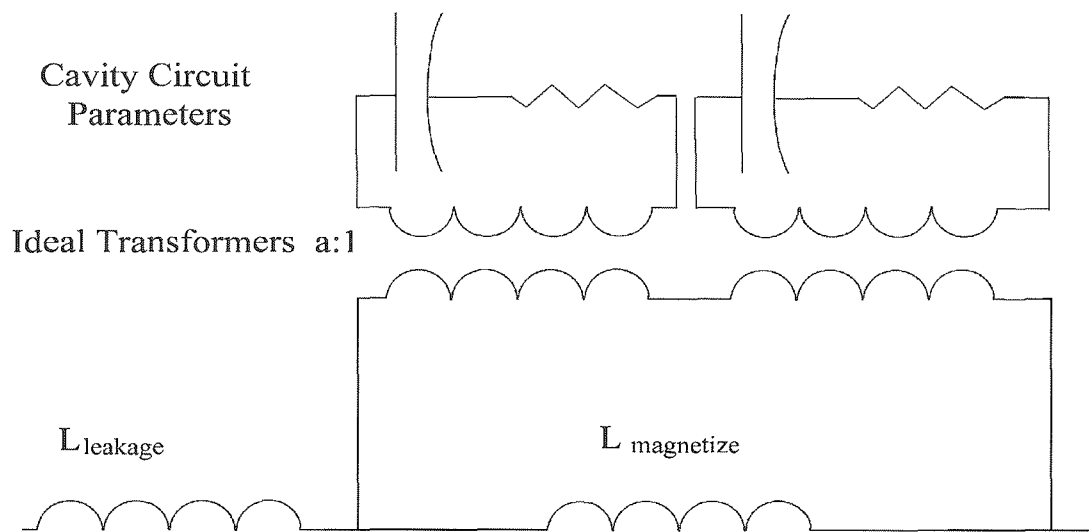


Figure 1-7. General coupling circuit model for coupling into a multiple-moded cavity.

$L_{\text{magnetize}}$ and L_{leakage} describe the self inductance of the coupling from either the charged particle beam or coupling wire into the cavity. The cavity parameters, C , L_{cavity} , and R are found by first determining a set of circuit terminals which couple to a particular cavity mode. Next, a volume integration of the electric and magnetic fields and a surface integration of the magnetic field uniquely determine C , L_{cavity} , and R , respectively.

The circuit of Fig. 1-7 may be simplified when the coupling to a particular set of modes is strong. Strong coupling implies that the leakage inductor may be neglected. Since accelerating cavities are designed to couple strongly to at least one

mode, the assumption that $L_{\text{leakage}} \approx 0$ is of practical

importance. The circuit in Fig. 1-7, subject to the assumption of strong coupling, results in the circuit of Fig.

1-8.

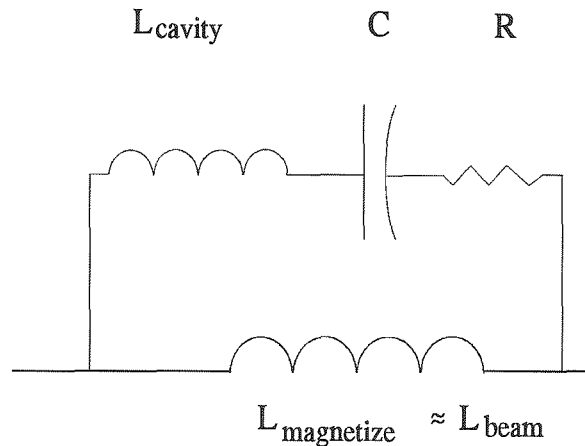


Figure 1-8. Equivalent circuit to Fig. 1-7 when the coupling to a particular mode is strong.

D. Review of Past Work

The wakefield is a phenomenon whose effects were known and observable long before they were directly measurable. One such facility which measured the wakefield was the Advanced Accelerator Test Facility (AATF) at Argonne National Laboratory (ANL). The AATF used a series of two short relativistic pulses of electric charge to measure the wakefield of the device under test (DUT). A high-energy excitation pulse of ~ 21 MeV was used to excite the wakefield in the DUT. The witness pulse, of lower energy (~ 15 MeV) and intensity for increased sensitivity, was affected by the resulting wake electric field from the excitation pulse after it passed through the DUT. The time between the two pulses was controlled and the difference in energy of the second pulse was recorded as a function of the time difference between the pulses. The energy difference of the witness pulse from before the discontinuity to after the discontinuity was theorized to be directly proportional to the wakefield of the DUT.

The measurement of the wakefield for a particular geometry is a complicated, expensive, and time-consuming procedure. It requires the following:

- ▶ A sufficiently strong disturbance (~ 10 keV) is required in the DUT for signal-to-noise (S/N) arguments. This requirement may demand a change in the desired

experiment in order to have a DUT which will induce a wakefield of sufficient magnitude. This necessary change adds variables and assumptions to the experiment. For example, a simple assumption made when using the AATF to measure a cavity whose wakefield is below the sensitivity of the AATF is: if one cavity produces a wakefield of magnitude M , then N cavities produce a wakefield of magnitude MN .

- ▶ The self-interaction of the witness pulse with the DUT is assumed to be negligible. Since both the excitation and witness pulses are relativistic, the physics *demands* that the witness pulse interact with the DUT in the same manner as the excitation pulse. Choosing the correct energy and intensity of the witness bunch, relative to the excitation bunch, was a primary design consideration for the AATF.
- ▶ A complicated structure and control system is required to control the time between the two pulses. This adds inherent design problems for particular time differences. The AATF, for example, had difficulty with the time difference $\Delta t=0$ since $\Delta t=0$ implies that both pulses are at the exact time and position as they pass through the DUT.
- ▶ The DUT must be adapted to the geometrical standards that the wakefield accelerator demands. This includes

changing dimensions of irises or beampipes from those of the DUT's original application to the beampipe or vacuum system dimensions required by the wakefield accelerator. These required changes may also change the loading on resonances in the DUT. Since the resonant frequencies of the DUT are dependent on the beampipe loading, the measured resonant frequencies of the DUT will be in error.

For a variety of reasons another method for estimating the wakefield was sought. One of the first papers addressing concerns of estimating the wakefield was written in 1974 by M. Sands and J. Rees [3], both from the Stanford Linear Accelerator Center (SLAC). Sands and Rees proposed using a wire to simulate a relativistic beam and gave estimates for regimes of validity for estimating the loss parameter. The technique of using a wire to simulate a relativistic beam is called the stretched wire measurement.

The stretched wire measurement gained popularity in experimental practice over the next ten years, and from 1985 to 1990 many theoretical papers were written for predicting the field structure for arbitrary discontinuities in the beampipe. Furthermore, experiments have shown that the stretched wire measurement has validity. Use of the stretched wire measurement to estimate the beam impedance can be desirable for several reasons. First, this type of

measurement can be performed relatively inexpensively with a highly sensitive network analyzer. The sensitivity of many commercially-available network analyzers is high enough such that a change in the experiment (i.e., adding cavities) is not necessary. Next, vacuum systems and problems associated with inserting the device into a wakefield accelerator are not encountered since the measurement is performed in air. Finally, the experiment can be effortlessly repeated several times if, as is usual, unforeseen experimental difficulties persist.

In 1985 H. Henke [4] from CERN solved the problem of a relativistic point charge moving along a circular beampipe which encounters either a pillbox cavity (see Fig. 1-9) or an infinite circular parallel plate waveguide (in Fig. 1-9, $b \rightarrow \infty$). The method of solution involved complex analysis to represent the magnetic field as a sum of all the waveguide modes in the beampipe, Hankel transforms of Maxwell's equations in r , the radial coordinate, and Fourier transforms in z . The magnetic fields were matched at the beampipe, and the solution was posed in the form of a Fourier series of the cavity modes. Henke also predicted the frequency response for the interaction of a Gaussian beam with the beam impedance and consequently he predicted the wakefield.

R. Gluckstern [5] expanded on Henke's work by expressing

the result for a general discontinuity in the form of an integral equation. His general method of solving a relativistic charge followed the same form as Henke's, but Gluckstern chose to solve Maxwell's equations without exploiting the Hankel transform that Henke used in his analysis. Gluckstern's resulting integral equation is

$$\int_0^g dz' F(z') [K_p(|z-z'|) + K_c(z, z')] = ie^{-ikz}, \quad (1-5)$$

where $F(z)$ is the unknown function which solves Eq. 1-5. $F(z')$ is defined explicitly by

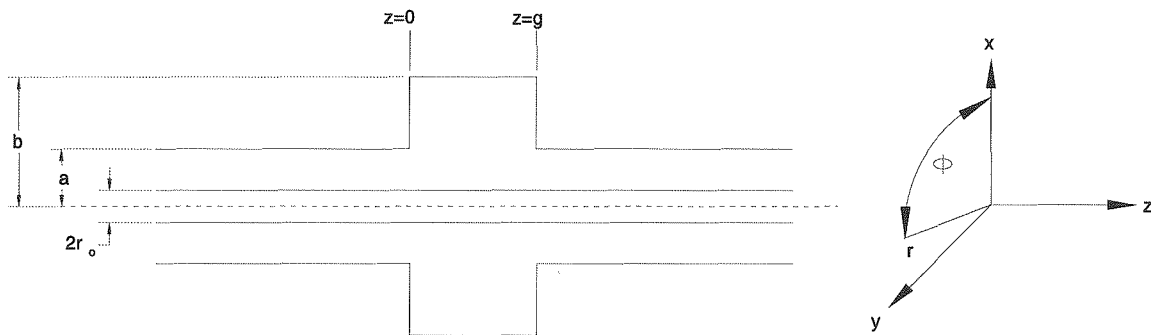


Figure 1-9. Consider an infinite structure leading into and out of a pillbox cavity.

$$F(z) = -\frac{Z_0 I_0}{ka^2} E_z(r=a, z) . \quad 16$$

$K_p(|z-z'|)$ is defined as the pipe kernel and is equal to

$$K_p(|z-z'|) = \frac{i2\pi}{a} \sum_{s=1}^{\infty} \frac{e^{\frac{-ib_s|z-z'|}{a}}}{b_s} , \quad (1-6)$$

where b_s is the wave number in z

$$b_s = \begin{cases} \sqrt{(ka)^2 - j_s^2} & j_s^2 < (ka)^2 \\ -i\sqrt{j_s^2 - (ka)^2} & j_s^2 > (ka)^2 \end{cases}$$

and the j_s 's are the solutions to $J_0(j_s)=0$. The complex number $i=\sqrt{-1}$. $K_c(z, z')$ is the cavity kernel and is equal to

$$K_c(z, z') = 4\pi^2 \sum_l \frac{h_l(r=a, z) h_l(r=a, z')}{k^2 - k_l^2} , \quad (1-7)$$

where $h_l(r, z)$ is the normalized magnetic field intensity for the l^{th} mode satisfying the perfect conducting boundaries defined by the square torus region $\{z: 0 \leq z \leq g; r: a \leq r \leq b\}$ depicted in Fig. 1-9. The normalization of the magnetic field intensity is

$$\vec{h}_l(r, z) = h_l(r, z) \hat{\Phi} = -iZ_0 \vec{H}_l(r, z) .$$

Using this normalization produces a symmetry in Maxwell's

equations:

$$\nabla \times \vec{E}_1 = k_1 \vec{H}_1 \quad \nabla \times \vec{H}_1 = k_1 \vec{E}_1,$$

where $k_1 = \frac{\omega_1}{c}$. Dimensional analysis shows that $\vec{H}_1(r, z)$ has the same units as the electric field. Additionally, $\vec{H}_1(r, z)$ and $\vec{E}_1(r, z)$ have the same normalization

$$\int_{cavity} \vec{E}_1 \cdot \vec{E}_m d\tau = \int_{cavity} \vec{H}_1 \cdot \vec{H}_m d\tau = \delta_{1,m}.$$

Finally, Gluckstern estimated the solution to his integral equation for high frequencies by modifying the kernels into their non-oscillatory components. The infinite summations of the non-oscillatory parts of the kernels can then be changed into integrations which are easily evaluated.

In 1989 Gluckstern and Li [6] solved the problem of placing a pulse of current on a coaxial wire of radius $r=r_0$ inside a pillbox cavity (see Fig. 1-9). This particular geometry is of special interest since it closely resembles a structure frequently used for estimating the beam impedance. Gluckstern and Li represent their solution in the same form as the integral equation in Eq. 1-5 where K_c , the cavity kernel, is the same as in the problem without the center conductor, while K_p , the pipe kernel, has an obvious difference due to a different beampipe geometry and is changed to

$$K_p(|z-z'|) = \frac{i2\pi}{a} \sum_{s=0}^{\infty} \frac{\alpha_s}{\tilde{b}_s} e^{\frac{-i\tilde{b}_s|z-z'|}{a}}, \quad (1-8)$$

where the α_s 's are defined by

$$\alpha_s = \frac{J_0^2\left(\frac{r_0 i_s}{a}\right)}{J_0^2\left(\frac{r_0 i_s}{a}\right) - J_0^2(i_s)} \quad s \geq 1, \quad \alpha_0 = \frac{1}{2 \ln\left(\frac{a}{r_0}\right)}, \quad (1-9)$$

and the i_s 's are the solutions to

$$Y_0(i_s) J_0\left(i_s \frac{r_0}{a}\right) - J_0(i_s) Y_0\left(i_s \frac{r_0}{a}\right) = 0 \quad s \geq 1. \\ i_0 \triangleq 0$$

The axial wave numbers are described similarly by

$$\tilde{b}_s = \begin{cases} \sqrt{(ka)^2 - i_s^2} & i_s^2 < (ka)^2 \\ -i\sqrt{i_s^2 - (ka)^2} & i_s^2 > (ka)^2 \end{cases}$$

Gluckstern and Li used the same techniques to solve the integral equation as Gluckstern used when he solved the problem of a relativistic charge encountering a pillbox cavity. The final conclusion from Gluckstern and Li concerns the similarity between the transmission coefficient $T(k)$ and the beam impedance $Z(k)$. They concluded that there exists a similarity between

$$\frac{Z(k)}{Z_0} \approx \frac{1 - T(k)}{2\pi\alpha_0}$$

for large k and small obstacles.

Gluckstern and Li found the transmission coefficient by first finding $E_z(r=a, z)$. They then found the scattered magnetic field through the relationship

$$Z_o H_\phi(r=a, z) = \frac{Z_o I_o}{2\pi a} e^{-ikz} - ik \int_{-\infty}^{\infty} A(q) e^{-iqz} J(q) dq. \quad (1-10)$$

The function $A(q)$ is defined by

$$A(q) \triangleq \frac{1}{2\pi} \int_0^g f(z) e^{iqz} dz$$

and

$$J(q) = -2 \sum_{s=0}^{\infty} \frac{\alpha_s}{q^2 a^2 - \tilde{b}_s^2}.$$

The integration of $A(q)$ in Eq. 1-10 is performed by complex analysis. The $s=0$ terms relate to the scattered transmitted and reflected magnetic field. The transmitted magnetic field is

$$H_\phi(r=a, z, \omega) = \begin{cases} \frac{I_o}{2\pi a} e^{-i\omega \frac{z}{c}} \left(1 + \frac{4\pi^2 \alpha_0 A(\frac{\omega}{c})}{Z_o I_o} \right) & z \geq g \\ \frac{2\pi \alpha_0}{a} A(-\frac{\omega}{c}) e^{i\omega \frac{z}{c}} & z < 0 \end{cases}.$$

They found the transmission coefficient by substituting the expression for $f(z)$ into $A(\frac{\omega}{c})$

$$T(\omega) = 1 + \frac{2\pi\alpha_0}{Z_o I_o} \int_0^g f(z) e^{i\omega \frac{z}{c}} dz. \quad (1-11)$$

In 1990 Heifets and Kheifets [7] from SLAC wrote a thorough theoretical paper discussing different iterative schemes for finding the beam impedance. Each iterative method is applied to a relativistic point charge interacting with a series of structures such as cavities and steps. They used the same technique of field matching to find the beam interactions and discussed methods of estimating high-order terms.

The final general ϕ -independent beampipe, cavity, and beam distribution integral equation which will be used throughout this dissertation is of the form

$$\frac{2\pi Z_o H_\phi^s(r=a, z)}{ika} = \int_0^g dz' f(z') \left(K_p(z-z') + K_c(z, z') \right). \quad (1-12)$$

This equation follows the exact formalism presented by Gluckstern et al. and only includes a minor difference in the form of the source term. Using this particular form of the integral equation will aid in studying realistic and practical geometries of stiff charged particle beams. The function $f(z)$ is the unknown function where $f(z) = E_z(r=a, z)$.

E. Goals

It is the purpose of this research to further investigate the stretched wire measurement and to present theoretical and experimental conclusions. To date only TM modes were analyzed and this dissertation will include all TM and transverse electromagnetic (TEM) cavity modes. With the aid of linear system theory, the derivation of a new integral equation will be presented. Furthermore, using the assumption of a particular source distribution, a different method for solving the problem of the interaction of the beam with its environment will be shown using a complex Fourier series approximation for $\vec{E}(r=a, z) \cdot \hat{z}$. With the complex Fourier series approximation, the effects of the coupling structure, namely the beampipe in the case of the physical particle beam or the wire in the case of the stretched wire measurement, can be extracted. Once the effects of the coupling structure are known, an objective comparative analysis between the effects can be made. Since the goal of the stretched wire measurement is to simulate a charged particle beam, an analysis between similar and dissimilar coupling structures should show where a regime of validity exists and for which frequencies the stretched wire measurement will adequately simulate an ultra-relativistic charged particle beam. With the Fourier series approximation, the theoretical solution of the stretched wire

measurement and wakefield measurement can finally be easily shown to converge to similar solutions.

II. Specific Source Considerations

A. Introduction

One technique used to estimate the beam impedance is the stretched wire measurement. This technique is used because the source fields of an ultra-relativistic bunch of charge are similar to an impulse of current on a center conductor. A review of these sources and their fields along with two other source geometries will be introduced.

Consider the geometry depicted in Fig. 1-9. Assume that the current source $\vec{J}(\vec{r}, t) = \vec{J}(r, z, t)$ or equivalently, assume that the source is independent of ϕ and all $\frac{\partial}{\partial \phi} \equiv 0$. Maxwell's equations, which are repeated below, must be satisfied everywhere in the beampipe and cavity regions.

$$\nabla \times \vec{E} = -\mu \frac{\partial \vec{H}}{\partial t} \quad \nabla \times \vec{H} = \epsilon \frac{\partial \vec{E}}{\partial t} + \vec{J}$$

B. Ultra-relativistic Point Charge

Assume that the source current is comprised of a charged particle of charge $q = I_0$ moving at the speed of light along the center of the beampipe. This source current has the form of Eq. 2-1:

$$\vec{J}(\vec{r}, t) = I_0 c \delta(z - ct) \frac{\delta(r)}{2\pi r} \hat{z}, \quad (2-1)$$

where the function $\delta(r)$ is the Dirac delta function and c is the speed of light. A current source in the form of Eq. 2-1

produces the following source fields [8], denoted by a superscript s :

$$\vec{E}^s(\vec{r}, t) = \frac{Z_o I_o C}{2\pi r} \delta(z-ct) \hat{r} \quad \vec{H}^s(\vec{r}, t) = \frac{I_o C}{2\pi r} \delta(z-ct) \hat{\phi},$$

where Z_o is the characteristic impedance of free space. Taking the Fourier transform¹ of Maxwell's equations with respect to time and using the current source in Eq. 2-1 results in the following electric and magnetic fields

$$\vec{E}^s(\vec{r}, \omega) = \frac{Z_o I_o}{2\pi r} e^{-ikz} \hat{r} \quad \vec{H}^s(\vec{r}, \omega) = \frac{I_o}{2\pi r} e^{-ikz} \hat{\phi}, \quad (2-2)$$

where $k = \frac{\omega}{c}$.

C. Impulse of Current on a Center Conductor

Consider the problem of an impulse of current with total charge $q = I_o$ traveling along a center conductor of radius r_o in the beampipe of Fig. 1-9. This source has the following form:

$$\vec{J}(\vec{r}, t) = I_o C \delta(z-ct) \frac{\delta(r-r_o)}{2\pi r} \hat{z}, \quad (2-3)$$

and will excite the following TEM mode:

$$\vec{E}^s(\vec{r}, t) = \frac{Z_o I_o C}{2\pi r} \delta(z-ct) \hat{r} \quad \vec{H}^s(\vec{r}, t) = \frac{I_o C}{2\pi r} \delta(z-ct) \hat{\phi}.$$

¹ See Appendix B for the definition of the Fourier transform and Fourier transform variables used in this manuscript.

The Fourier-transformed source fields are

$$\vec{E}^s(\vec{r}, \omega) = \frac{Z_o I_o}{2\pi r} e^{-ikz} \hat{r} \quad \vec{H}^s(\vec{r}, \omega) = \frac{I_o}{2\pi r} e^{-ikz} \hat{\phi}. \quad (2-4)$$

By comparing Eqs. 2-2 and 2-4 one concludes that the source fields of an ultra-relativistic charged particle and the source fields of an impulse of current on a wire are indistinguishable. The fact that the source fields are the same between the wire and relativistic beam gave Sands and Rees [3] the notion to use a SWM to estimate the wakefield.

D. Ultra-relativistic Gaussian Bunch

Consider the ultra-relativistic Gaussian bunch with total charge $q=I_o$. For this source

$$\vec{J}(\vec{r}, t) = \frac{I_o C}{\sigma \sqrt{\pi}} e^{-\left(\frac{z-ct}{\sigma}\right)^2} \frac{\delta(r)}{2\pi r} \hat{z}. \quad (2-5)$$

The Fourier-transformed source and its fields are

$$\vec{J}(\vec{r}, \omega) = \frac{I_o}{Z_o} e^{-ikz} e^{-\left(\frac{k\sigma}{2}\right)^2} \frac{\delta(r)}{2\pi r} \hat{z}, \quad (2-6)$$

$$\vec{E}^s(\vec{r}, \omega) = \frac{Z_o I_o}{2\pi r} e^{-ikz} e^{-\left(\frac{k}{2\sigma}\right)^2} \hat{r}, \quad \vec{H}^s(\vec{r}, \omega) = \frac{I_o}{2\pi r} e^{-ikz} e^{-\left(\frac{k}{2\sigma}\right)^2} \hat{\phi}. \quad (2-7)$$

The importance of Eq. 2-7 is the similarity in the z dependence of the fields to the case of the impulse of

current. The salient difference in the transformed fields between the impulse of current and the Gaussian bunch is the attenuation of the fields for the Gaussian bunch with increasing frequency.

E. Ultra-relativistic Time-Limited-Cosine-Squared Bunch

Consider the time-limited-cosine-squared current distribution

$$\vec{J}(\vec{r}, t) = \frac{-I_0 \kappa^2 \sigma^2}{4\pi^2 c^2} \cos^2\left(\frac{\pi(z-ct)}{\kappa\sigma}\right) \left(u\left(z-ct+\frac{\kappa\sigma}{2}\right) - u\left(z-ct-\frac{\kappa\sigma}{2}\right)\right) \frac{\delta(r)}{2\pi r} \hat{z} \quad (2-8)$$

where the function $u(z)$ is the Heaviside step function

$$u(z) = \begin{cases} 1 & z \geq 0 \\ 0 & z < 0 \end{cases},$$

and of total charge $q = I_0 \frac{\kappa\sigma}{c}$. The parameter κ is chosen such that this distribution most closely resembles the Gaussian distribution described in Eq. 2-5. This was accomplished by minimizing the following function of κ :

$$\int_{-\frac{\kappa\sigma}{2}}^{\frac{\kappa\sigma}{2}} \left(e^{-\left(\frac{z}{\sigma}\right)^2} - \cos^2\left(\frac{\pi z}{\kappa\sigma}\right) \right)^2 dz.$$

The minimum κ was found numerically and is equal to $\kappa = 3.517868$. This value will be used throughout the remainder

of this dissertation. A graph of a particular Gaussian ($\sigma=4.0\text{mm}$) and a time-limited-cosine-squared current distribution ($\sigma=4.0\text{mm}$, $\kappa=3.517868$) is shown in Fig. 2-1. Each current source in Fig. 2-1 is normalized to contain an equal charge of $q=2.31\times 10^{-9}\text{C}$. The important feature of Fig. 2-1 is the similarity of the two current distributions using the minimum κ . Additionally, Fig. 2-1 shows the tails of the Gaussian decaying as $z\rightarrow\pm\infty$ and the time/space limitation of the cosine-squared source at $z=\pm\frac{\kappa\sigma}{2}\approx\pm 0.0067\text{ mm}$.

The Fourier transform of the time-limited-cosine-squared current distribution of Eq. 2-8 is

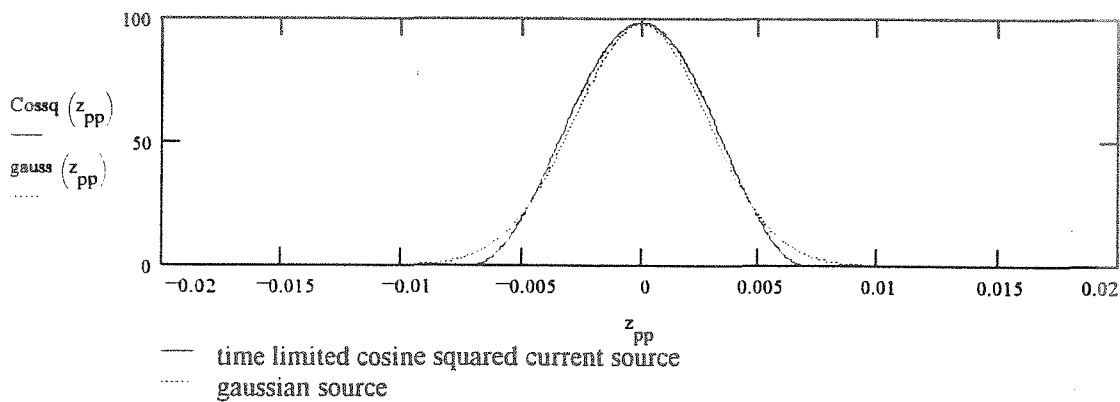


Figure 2-1. A plot of the spatial dependence (mm) for equal charge current distributions of a time-limited-cosine-squared source of Eq. 2-8 using the minimum κ and $\sigma=4\text{mm}$ versus a Gaussian current source of Eq. 2-5 with $\sigma=4\text{mm}$.

$$\vec{J}(\vec{r}, \omega) = I_o \frac{\sin\left(\frac{\omega \kappa \sigma}{2c}\right) e^{-i\omega \frac{z}{c}}}{\omega \left(\omega^2 - \left(\frac{2\pi c}{\kappa \sigma} \right)^2 \right)} \frac{\delta(r)}{2\pi r} \hat{z}$$

and the Fourier-transformed electric and magnetic fields for the time-limited-cosine-squared current source are

$$\vec{E}^s(\vec{r}, \omega) = \frac{Z_o I_o}{2\pi r} \frac{\sin\left(\frac{\omega \kappa \sigma}{2c}\right) e^{-ikz}}{\omega \left(\omega^2 - \left(\frac{2\pi c}{\kappa \sigma} \right)^2 \right)} \hat{r} \quad (2-9)$$

and

$$\vec{H}^s(\vec{r}, \omega) = \frac{I_o}{2\pi r} \frac{\sin\left(\frac{\omega \kappa \sigma}{2c}\right) e^{-ikz}}{\omega \left(\omega^2 - \left(\frac{2\pi c}{\kappa \sigma} \right)^2 \right)} \hat{\phi}.$$

F. Summary

The source fields presented in this chapter are the *particular* solutions to Maxwell's equations. The complete solution adds to these fields the homogeneous solution (where the source $\vec{J}=0$) which will satisfy the boundary conditions

everywhere. The remainder of this dissertation discusses how one finds the homogeneous solution and comments on the validity of the calculated solution.

III. Determination of a New Integral Equation

Using simple linear system theory Eq. 1-12 can be cast into a different form. The effect of all the cavity modes on the integral equation in Eq. 1-12 will be pointed out. It is an additional goal of this chapter to point out the steps to the realization of a new integral equation. The new integral equation turns out to be rather complicated and will not be solved.

A. Background Definitions

To represent the location of the cavity resonator (see Fig. 1-9) it is necessary to define a new function $u_g(z)$:

$$u_g(z) = u(z) - u(z-g),$$

where $u(z)$ is the Heaviside step function defined in Ch. II. The function $u_g(z)$ is therefore

$$u_g(z) = \begin{cases} 1 & z \in [0, g] \\ 0 & z \notin [0, g] \end{cases}.$$

Note that this new function $u_g(z)$ has the convenient property that $u_g(z) = u_g(z)u_g(z)$. Taking the Fourier transform of $u_g(z)$ with respect to z shows: $U_g(q) = \mathcal{F}\{u_g(z)\}_z = \mathcal{F}\{u_g(z)u_g(z)\}_z = \frac{1}{2\pi}U_g(q) \otimes U_g(q)$. The \otimes symbol represents the convolution operation.

B. Derivation of Equation

The integral equation derived by Gluckstern may be transformed into another integral equation using simple

properties of the Fourier transform; this new integral equation suggests a new method for estimating the solution with linear algebra.

Upon close examination of the cavity kernel $K_c(z, z')$ in Eq. 1-7, the transformed integral equation can be arrived at in a fairly straightforward manner.

In Eq. 1-7, $h_1(r, z)$ is the normalized magnetic field for a particular mode of the coaxial cavity depicted in Fig. 3-1, with length g , and inner and outer conductors of radii a and b , respectively. Note that with these definitions, the cavity region is identical in both the problem with the center conductor and with a physical beam.

The TM modes for the cavity depicted in Fig. 3-1 have the following field structure ($l=0, 1, 2, 3, \dots$; $m=1, 2, 3, \dots$):

$$\vec{E}_{l,m} \cdot \hat{z} = \frac{A_{l,m} \beta_m c}{\omega \sqrt{\pi g}} \left(Y_0(\beta_m a) J_0(\beta_m r) - J_0(\beta_m a) Y_0(\beta_m r) \right) \cos\left(\frac{l\pi z}{g}\right),$$

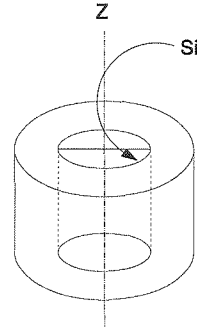


Figure 3-1. The ϕ -independent discontinuity or cavity region. The cavity region is chosen such that it lies exterior to the beam pipe region. This effectively makes the cavity modes independent of the geometry exterior to the cavity.

$$\vec{E}_{1,m} \cdot \hat{r} = \frac{A_{1,m} C \sqrt{\pi}}{\omega g^{3/2}} \left(Y_0(\beta_m a) J_1(\beta_m r) - J_0(\beta_m a) Y_1(\beta_m r) \right) \sin\left(\frac{l\pi z}{g}\right), \quad (3-1)$$

$$\begin{aligned} -iZ_o \vec{H}_{1,m} \cdot \hat{\Phi} &= h_{1,m}(r, z) = \\ &= \frac{A_{1,m}}{\sqrt{\pi g}} \left[J'_0(\beta_m r) Y_0(\beta_m a) - Y'_0(\beta_m r) J_0(\beta_m a) \right] \cos\left(\frac{l\pi z}{g}\right) u_g(z), \end{aligned}$$

where the β_m 's solve $J_0(\beta_m b) Y_0(a) - Y_0(\beta_m b) J_0(\beta_m a) = 0$ and the $A_{1,m}$'s are defined by

$$\begin{aligned} A_{1,m} &= \frac{1}{\sqrt{\int_{cavity} \vec{H}_{1,m} \cdot \vec{H}_{1,m}^* d\tau}} \\ &= \frac{1}{\sqrt{\left(1 + \delta_{l,0}\right) \int_a^b r \left(J_0(\beta_m a) Y_1(\beta_m r) - Y_0(\beta_m a) J_1(\beta_m r) \right)^2 dr}}. \end{aligned}$$

The resonant frequencies of the TM cavity modes are

$$\omega_{1,m}^2 = c^2 \left(\beta_m^2 + \left(\frac{l\pi}{g} \right)^2 \right).$$

The TEM modes in this annular region have the following field structure:

$$-iZ_o \vec{H}_l(r, z) \cdot \hat{\Phi} = h_l(r, z) = \frac{1}{r \sqrt{\pi g \ln\left(\frac{b}{a}\right)}} \cos\left(\frac{\pi l z}{g}\right) u_g(z), \quad (3-2)$$

$$\vec{E}_1(r, z) = \hat{r} \frac{1}{\sqrt{g\pi \ln\left(\frac{b}{a}\right) r}} \sin\left(\frac{l\pi z}{g}\right) u_g(z).$$

The TEM resonant frequencies are

$$\omega_l^2 = c^2 \left(\frac{l\pi}{g}\right)^2$$

and $l=\{1,2,3,\dots\}$. An additional mode is necessary to accommodate the energy storage of the DC fields [9]. The normalized magnetic field distribution is

$$h_l(r, z) = \frac{1}{\sqrt{2\pi g \ln\left(\frac{b}{a}\right) r}}. \quad (3-3)$$

Applying the TM and TEM definitions from Eqs. 3-1, 3-2, and 3-3 for the $h_l(r, z)$ shows that the cavity kernel in Eq. 1-7 is specifically dependent on a product of cosine terms of equal frequency. By using a trigonometric identity that the product of cosines is a modulator

$$\cos(\lambda) \cos(v) = \frac{1}{2} [\cos(\lambda - v) + \cos(\lambda + v)],$$

the cavity kernel can be rewritten into a sum of cosines rather than a product of cosines. Consider rewriting the cavity kernel into a functional form, replacing the infinite sum of cosine terms with the functions $h(z-z')$ and $h(z+z')$. Rewriting the right-hand side (RHS) of Eq. 1-12 using this

functional form of the cavity kernel shows

$$\int_{-\infty}^{\infty} dz' f(z') u_g(z') [K_p(|z-z'|) + (h(z-z') + h(z+z'))]. \quad (3-4)$$

Equation 3-4 is expressed in a format similar to a convolution integral. Convolution integrals have the property that they may be transformed into a simple multiplication operation with the aid of the Fourier transform. Consider taking the spatial Fourier transform of Eq. 3-4 with respect to z , resulting in

$$F(q) \hat{K}_p(q) + \frac{1}{2\pi} F(q) H(q) \otimes U_g(q) + \frac{1}{2\pi} U_g(q) \otimes \mathcal{F}\left(\int_{-\infty}^{\infty} f(z') h(z+z') dz'\right)_z.$$

The quantity $\mathcal{F}\left(\int_{-\infty}^{\infty} f(z') h(z+z') dz'\right)_z$ is outlined in Appendix C and is $F(-q)H(q)$.

Taking the Fourier transform of Eq. 3-4 results in

$$\mathcal{F}\left\{\frac{2\pi Z_0 H_\phi^s(r=a, z)}{ika}\right\}_z = \frac{2\pi Z_0 H_\phi^s(r=a, q)}{ika} = F(q) \hat{K}_p(q) + \frac{1}{2\pi} U_g(q) \otimes [F(q) + F(-q)] H(q). \quad (3-5)$$

In Eq. 3-5 the unknown quantity to solve for is $F(q)$. It is evident that the original integral equation is now transformed into a new integral equation. This equation

shows some interesting properties. First, only the even part of $F(q)$ contributes to the cavity interaction, which is only a consequence of the choice in the definition for the cavity location along the z axis. Next, note that since $H(q)$ is the Fourier transform of a cosine function, $H(q)$ is comprised of two delta functions. Furthermore, the convolution of $F(q)H(q)$ with $U_g(q)$ effectively generates a sum of shifted $U_g(q)$, each scaled by a sampled $F(q)$ at each of the eigenmodes of the cavity. This makes Eq. 3-5 a difficult equation to solve for $F(q)$. The fact that $F(q)$ is sampled at the cavity resonant frequencies suggests using a Fourier series technique to solve the original integral equation in Eq. 1-12. The Fourier series technique will be presented in Ch. IV. It is not apparent, however, how to readily solve the new integral equation. Perhaps with the use of other transformations and mathematical manipulations the new integral equation may be solved. One of these analytical techniques which may solve Eq. 3-5 is called collocation [10].

IV. Charged Particle Beam Solution

A. Theoretical Solution to the Integral Equation

A method of estimating the solution to the integral equation in Eq. 1-12 using a Fourier series technique is introduced. This technique takes advantage of the orthogonality and completeness of the set of $e^{i\frac{2l\pi z}{g}}$ terms for a bounded interval of length g . Applying standard Fourier series techniques, make the following definition:

$$f(z, \omega) \triangleq \sum_{l=-\infty}^{\infty} \gamma_l(\omega) e^{i\frac{2l\pi z}{g}} u_g(z), \quad (4-1)$$

where $f(z, \omega) = E_z(r=a, z, \omega)$. The presence of $u_g(z)$, defined in Ch. III, says that the representation of $f(z)$ by the Fourier series is to take place on the interval $\{0 \leq z \leq g\}$. Multiplying Eq. 1-12 by $e^{-i\frac{2p\pi z}{g}}$ and integrating z over $\{0 \leq z \leq g\}$ while using the definition of Eq 4-1 for $f(z, \omega)$, the pipe kernel term on the RHS of Eq. 1-12 becomes

$$\begin{aligned} \int_0^g dz \int_0^g dz' f(z') K_p(z-z') e^{-i\frac{2p\pi z}{g}} = \\ \int_0^g dz \int_0^g dz' \sum_{l=-\infty}^{\infty} \gamma_l e^{i\frac{2l\pi z'}{g}} K_p(|z-z'|) e^{-i\frac{2p\pi z}{g}} \end{aligned} \quad (4-2)$$

Assuming that this summation is uniformly convergent for $\{0 \leq z \leq g, 0 \leq z' \leq g\}$, it is therefore possible to pull the

summation out of the integrand, resulting in the following equation:

$$= \sum_{l=-\infty}^{\infty} \gamma_l \int_0^g dz \int_0^g dz' e^{\left(i \frac{2l\pi z'}{g}\right)} K_p(|z-z'|) e^{\left(-i \frac{2p\pi z}{g}\right)}.$$

For compact writing, make the following definitions:

$$\theta_{l,p} \triangleq \int_0^g dz \int_0^g dz' e^{\left(i \frac{2l\pi z'}{g}\right)} K_p(|z-z'|) e^{\left(-i \frac{2p\pi z}{g}\right)}, \quad (4-3)$$

$$\underline{\underline{\Theta}} \triangleq \begin{bmatrix} \dots & \vdots & & & \vdots \\ \dots & \theta_{0,0} & \theta_{1,0} & \dots & \theta_{l,0} & \dots \\ \dots & \theta_{0,1} & \theta_{1,1} & \dots & \theta_{l,1} & \dots \\ \dots & \vdots & & & \vdots \\ \dots & \theta_{0,p} & \theta_{1,p} & \dots & \theta_{l,p} & \dots \\ \dots & \vdots & & & \vdots \end{bmatrix} \quad \underline{\underline{\Gamma}} \triangleq \begin{bmatrix} \vdots \\ \gamma_0 \\ \gamma_1 \\ \vdots \\ \gamma_p \\ \vdots \end{bmatrix}.$$

The formulae for the $\theta_{l,p}$ and integrals which aid in both the calculation and the asymptotics of Eq. 4-3 are listed in Appendix D. Using this notation, the RHS of Eq. 4-2 may be rewritten as $\sum_{l=-\infty}^{\infty} \gamma_l \theta_{l,p}$, or the p^{th} row vector of $\underline{\underline{\Theta}}$ multiplied by the column vector $\underline{\underline{\Gamma}}$.

Now consider the influence of the cavity kernel. The

cavity contribution is solved for by substituting the appropriate sum from the terms in Eqs. 3-1, 3-2, and 3-3 into the definition of the cavity kernel in Eq. 1-7. Multiplying the cavity kernel by $e^{-i\frac{2p\pi z}{g}}$ and integrating z over $\{0 \leq z \leq g\}$ results in

$$\int_0^g dz \int_0^g dz' f(z') K_c(z, z') e^{-i\left(\frac{2p\pi z}{g}\right)} = \int_0^g dz \int_0^g dz' \sum_{l=-\infty}^{\infty} \gamma_l e^{i\left(\frac{2l\pi z}{g}\right)} K_c(z, z') e^{-i\left(\frac{2p\pi z}{g}\right)}. \quad (4-4)$$

Again, assume that the integral in Eq. 4-4 is uniformly convergent for $\{0 \leq z \leq g, 0 \leq z' \leq g\}$, and it is therefore possible to pull the summation over l out of the integral. For compact writing, make the following definitions:

$$\xi_{l,p} \triangleq \int_0^g dz \int_0^g dz' e^{i\left(\frac{2l\pi z'}{g}\right)} K_c(z, z') e^{-i\left(\frac{2p\pi z}{g}\right)},$$

$$\Xi \triangleq \begin{bmatrix} \dots & \vdots & & & \vdots \\ \dots & \xi_{0,0} & \xi_{1,0} & \dots & \xi_{1,0} & \dots \\ \dots & \xi_{0,1} & \xi_{1,1} & \dots & \xi_{1,1} & \dots \\ \dots & \vdots & & & \vdots \\ \dots & \xi_{0,p} & \xi_{2,p} & \dots & \xi_{1,p} & \dots \\ \dots & \vdots & & & \vdots \end{bmatrix}. \quad (4-5)$$

The formulae for the $\xi_{1,p}$ and integrals which aid in both the calculation and asymptotics of Eq. 4-4 are listed in Appendix D. Using this definition, the RHS of Eq. 4-4 is simply

$$\sum_{l=-\infty}^{\infty} \gamma_l \xi_{l,p}.$$

The final term to insert into the complex Fourier-analysis is the left-hand side (LHS) of Eq. 1-12, which defines the source of excitation. Designate the quantity

$$\varphi_p \triangleq \frac{2\pi Z_0}{ik a} \int_0^g dz \vec{H}_\phi^s(r=a, z, \omega) \cdot \hat{z} e^{-i\left(\frac{2p\pi z}{g}\right)}, \quad (4-6)$$

where $\vec{H}_\phi^s(r=a, z, \omega)$ is the magnetic field intensity for a particular source distribution (e.g., Eqs. 2-2, 2-4, 2-7, or 2-9). Using the definition for φ_p in Eq. 4-6, define the vector $\underline{\Phi}$

$$\underline{\Phi} \triangleq \begin{bmatrix} \vdots \\ \varphi_0 \\ \varphi_1 \\ \vdots \\ \varphi_p \\ \vdots \end{bmatrix}.$$

At this point the integral equation may be rewritten into an infinite-dimensional linear equation. By applying the

definitions of the matrices $\underline{\underline{\Theta}}$ and $\underline{\underline{E}}$, and the vectors $\underline{\Phi}$ and $\underline{\Gamma}$, an equation is obtained which defines the unknown vector $\underline{\Gamma}$

$$(\underline{\underline{\Theta}} + \underline{\underline{E}})\underline{\Gamma} = \underline{\Phi}. \quad (4-7)$$

Equation 4-7 is an infinite-dimensional linear equation in $\underline{\Gamma}$. The entire dependence of the pipe structure is contained in the matrix $\underline{\underline{\Theta}}$, the cavity dependence in the matrix $\underline{\underline{E}}$, and the source in the vector $\underline{\Phi}$. Equation 4-7 is valid for any geometry of excitation source under two conditions: the source geometry must be ϕ -independent and the source must have a Fourier transform. Using the formalism introduced by Gluckstern in either of Eqs. 1-6 or 1-8 for the pipe kernel and Eq. 1-7 for the cavity kernel, each element of the matrices $\underline{\underline{\Theta}}$ and $\underline{\underline{E}}$ is stated in Appendix D. Equation 4-7 represents a new form of the integral equation dictated in Eq. 1-12. The linear equation of Eq. 4-7 may be relatively easily solved and converges uniformly to the solution of Eq. 1-12.

B. Considerations for Calculating the Beam Impedance

i. Choosing the Dimension to the Linear Equation

The infinite-dimensional matrix equation in Eq. 4-7 obviously cannot be solved exactly and must therefore be estimated. Choosing the dimension of the matrix turns out to be a function of the frequency range that is desired for the solution, which in turn is a function of the source excitation. In this dissertation, the spectrum of the beam

impedance was calculated to 70 GHz since a Gaussian source distribution was assumed with $\sigma=4.0\text{mm}$. The dimension p of the matrices and vectors were chosen to satisfy the following criteria:

$$\frac{2p\pi}{g} \gg k_{\text{highest}}.$$

Since this analysis uses the complex Fourier series, negative elements must be allowed into the solution. Adding the negative components raises the final dimension of the vectors, for example, to $2p+1$. The final dimension for the calculations contained herein is 15×15 for the matrices and likewise 15×1 for the vectors.

ii. Choosing the Frequencies and Number of Frequency Points

Simply calculating the beam impedance accurately over the required 70-GHz bandwidth posed a problem since it is possible to completely skip cavity modes by not carefully choosing the correct frequencies to solve the matrix equation. A linear frequency span of 525 data points from 1 Hz to 70 GHz was first chosen. Then, frequencies near the cavity resonant frequencies were added and the results were concatenated. This turned out to have an important effect on the modes below the first cutoff frequency of the beampipe and did not seem to change the results for frequencies higher than the first cutoff frequency of the beampipe. The reason for this is that the above-cutoff cavity modes are

essentially "de-Q'd" and mathematically do not behave as violently in the vicinity of the resonance as do the cavity modes below cutoff.

iii. Perfect Conducting Boundary Considerations

An important practical consequence arises from solving a perfect conducting cavity system below cutoff [11]. This can be likened to solving a circuit problem similar to the coupled resonator circuit without the loss resistor depicted in Fig. 1-8; this is shown in Fig. 4-1. The impedance of the perfect conducting coupled resonator circuit is readily found:

$$Z(\omega) = \frac{i\omega L_{couple}}{1 - \omega^2 C(L_{cavity} + L_{couple})} - \frac{i\omega^3 L_{cavity} L_{couple} C}{1 - \omega^2 C(L_{cavity} + L_{couple})}. \quad (4-8)$$

This particular $Z(\omega)$ has no inverse Fourier transform or impulse response for two reasons. First, the right-hand term of Eq. 4-8 grows without bound as $\omega \rightarrow \infty$. The physical solution is not affected by this result since the model of Fig. 4-1 is both band limited and only assumes

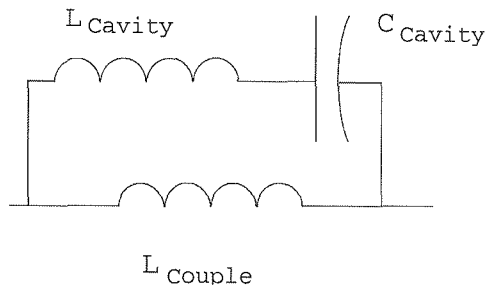


Figure 4-1. Below cutoff representation for cavity coupling circuit.

a single mode. The existence of multiple modes causes the high frequency inductance of the right-hand term to couple to the higher frequency cavity modes [12]. Additionally, the integral equation in Eq. 1-12 controls the coupling mechanism, which is a function of frequency and not simply an inductor as depicted in Fig. 4-1. Second, the left-hand term in Eq. 4-8, which describes the parallel resonant nature of the circuit, requires that the resonant frequency

$$\omega_o = \frac{1}{\sqrt{C(L_{cavity} + L_{couple})}}$$

be complex for the inverse Fourier transform to exist. This particular term posed a problem for verifying the work contained in this dissertation because Simpson et al. recorded the experimental data in the time domain while the numerical analysis was done in the frequency domain. Using Fourier transform techniques, a method of taking the theoretical data back to the time domain was sought. If one were to naively take the numerical inverse Fourier transform of the unmodified perfect conducting $Z(\omega)$ in an attempt to find the impulse response, it would be apparent from finding non-causal results that a problem exists in the calculated time domain data.

Modifying the computed data near the parallel resonant frequency solved the problem of computing the wakefield. This modification was performed by comparing the response of the ideal problem depicted in Fig. 4-1 to that of a more realistic coupled resonator problem

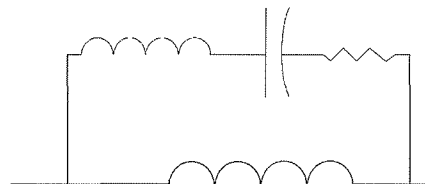


Figure 4-2. Non-ideal circuit equivalent of Fig. 4-1. This circuit was used to modify the beam impedance response for below cutoff cavity modes.

shown in Fig. 4-2. For this circuit, $Z(\omega)$ takes on the form

$$Z(\omega) = \frac{i\omega^3 L_{\text{cavity}} L_{\text{couple}} C + \omega^2 L_{\text{couple}} RC - i\omega L_{\text{couple}}}{\omega^2 C (L_{\text{cavity}} + L_{\text{couple}}) - i\omega RC - 1}. \quad (4-9)$$

The inverse Fourier transform of the impedance in Eq. 4-9 does not exist. Examination of $Z(\omega)$ for large ω shows that $Z(\omega)$ grows without bound. Similar arguments used in the circuit of Fig. 4-1 explains that this effect can be neglected. The prominent difference between Figs. 4-1 and 4-2 is the existence of a real resonant frequency for Fig. 4-1 and a complex resonant frequency for Fig. 4-2. The complex resonant frequency assures that the excited fields will evanesce and the inverse Fourier transform will then exist. The resistor in Fig. 4-2 is chosen such that the cavity parameter Q is comparable to the Q of the resonance of the

cavity without the beampipes attached. Q 's on the order of 15,000 were used to modify the calculated ideal beam impedance in this analysis. The cavity inductance was calculated by an appropriate integration of the magnetic field and the capacitance was calculated by an integration of the electric field. The net effect of this modification is the addition of a real part to the beam impedance in a small frequency range near the cavity eigenmodes. The imaginary parts of the impedance were not modified with this circuit model. Modification of the computed data is not necessary for the cavity modes whose frequencies are higher than the first cutoff frequency of the beampipe.

C. Computational Results

i. Assumptions

The computations outlined below for the geometry depicted in Fig. 1-9 were done with the intention of simulating the measurement made by Simpson [13]. The dimensions for this particular simulation are:

- Gaussian Beam -- waist (σ) = 4.0 mm
- Charge in the Bunch (q) = 2.31 nC
- Length of Cavity (g) = 0.32 cm
- Cavity Outer Diameter (b) = 1.95 cm
- Beampipe Diameter (a) = 0.63 cm
- Number of Cavities = 103

The errors caused by truncating the infinite sums in Eqs. D-1 through D-6 for both the cavity and pipe modes have been estimated in the analysis. It is also assumed that the wakefield for 'n' cavities is simply the instantaneous superposition of 'n' wakefields. This clearly is a major assumption and perhaps explains the discrepancies between the measurement and the simulation.

ii. Perfect Conducting Boundary Modification

Figure 4-3 is a plot of the calculated beam impedance. The first two spikes of impedance occur near 6 GHz and 15 GHz, which are a result of the first two TM cavity modes. These two cavity modes required the addition of a real component to the beam impedance in the vicinity of the resonance and the resulting graph is shown in Fig. 4-4.

Another prominent feature of the beam impedance, which occurs near 18 GHz, is caused by the excitation of the first propagating pipe mode. The existence of a positive real part to the beam impedance is calculated as expected for all frequencies above the first pipe cutoff frequency. The computed wakefield for the beam impedance in Fig. 4-4, with the aforementioned Gaussian current source, is shown in Fig. 4-5.

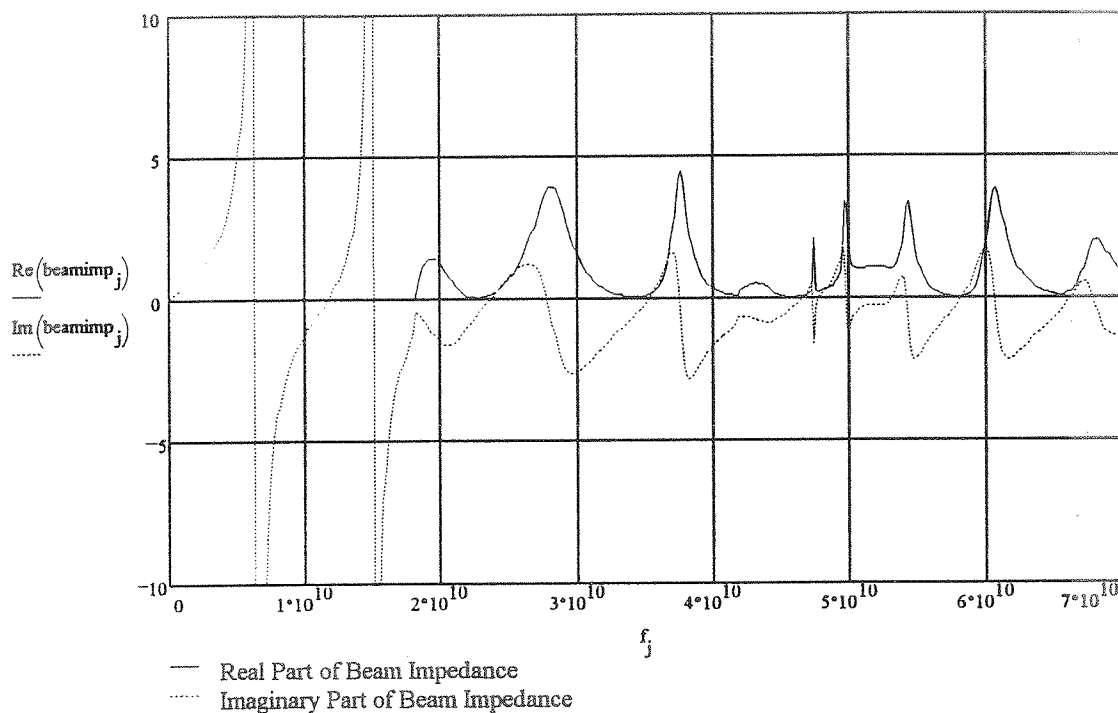


Figure 4-3. The beam impedance (Ω) as a function of frequency (Hz) for the structure described in Fig. 1-9 with $a=0.63$ cm, $b=1.95$ cm, and $g=0.32$ cm.

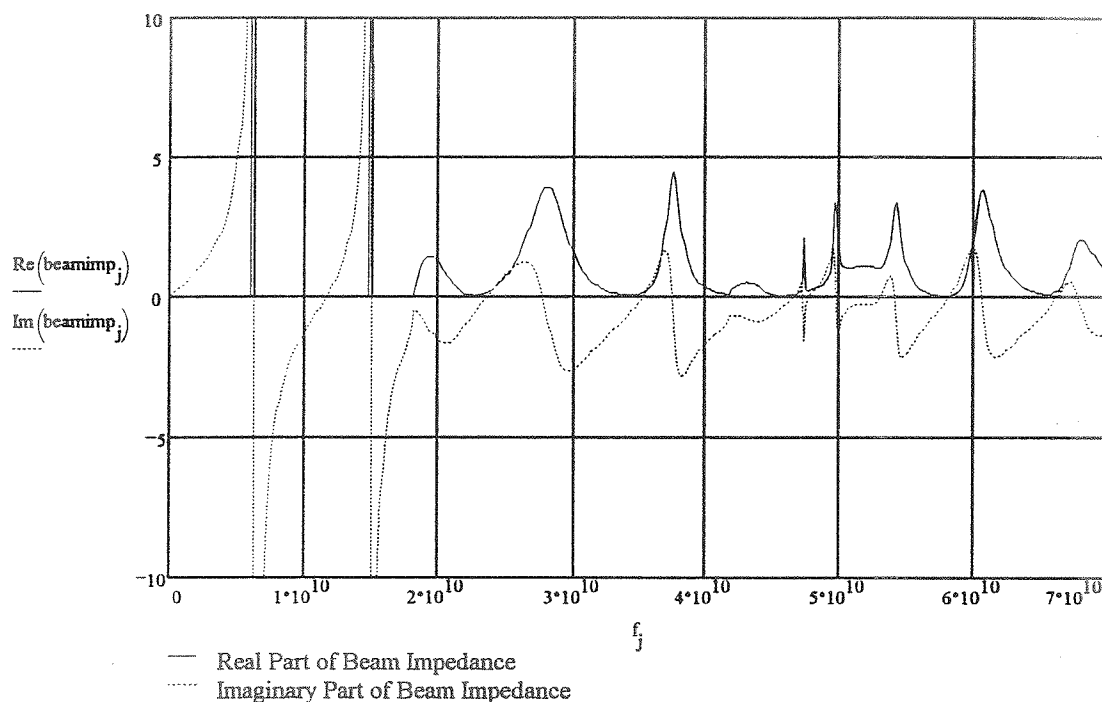


Figure 4-4. Corrected beam impedance (Ω) calculation includes the addition of a real component to the beam impedance at the first two cavity resonances.

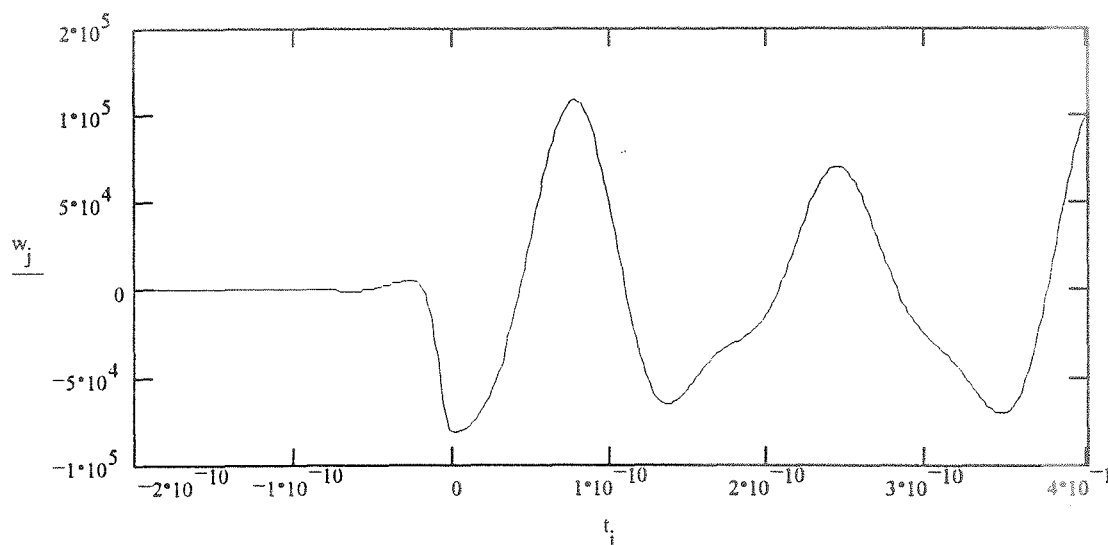


Figure 4-5. The calculated wakefield (eV) for the Simpson experiment described in Ch. IV.C.i. versus time (s).

iii. Comparison of Theory to Measurement

A plot from the actual measurement made by Simpson is shown in Fig. 4-6. The differences between the actual experiment and the theoretical analysis were carefully considered and the explanations of the measurement and measurement technique were studied. The relative magnitudes and phases between Figs. 4-5 and 4-6 show reasonable agreement and provide evidence that the method presented to solve Eq. 1-12 with the complex Fourier series is justified.

Simpson's experiment was comprised of 103 resonant pillbox cavities. Each cavity had to be individually machined and, therefore, each cavity was slightly different

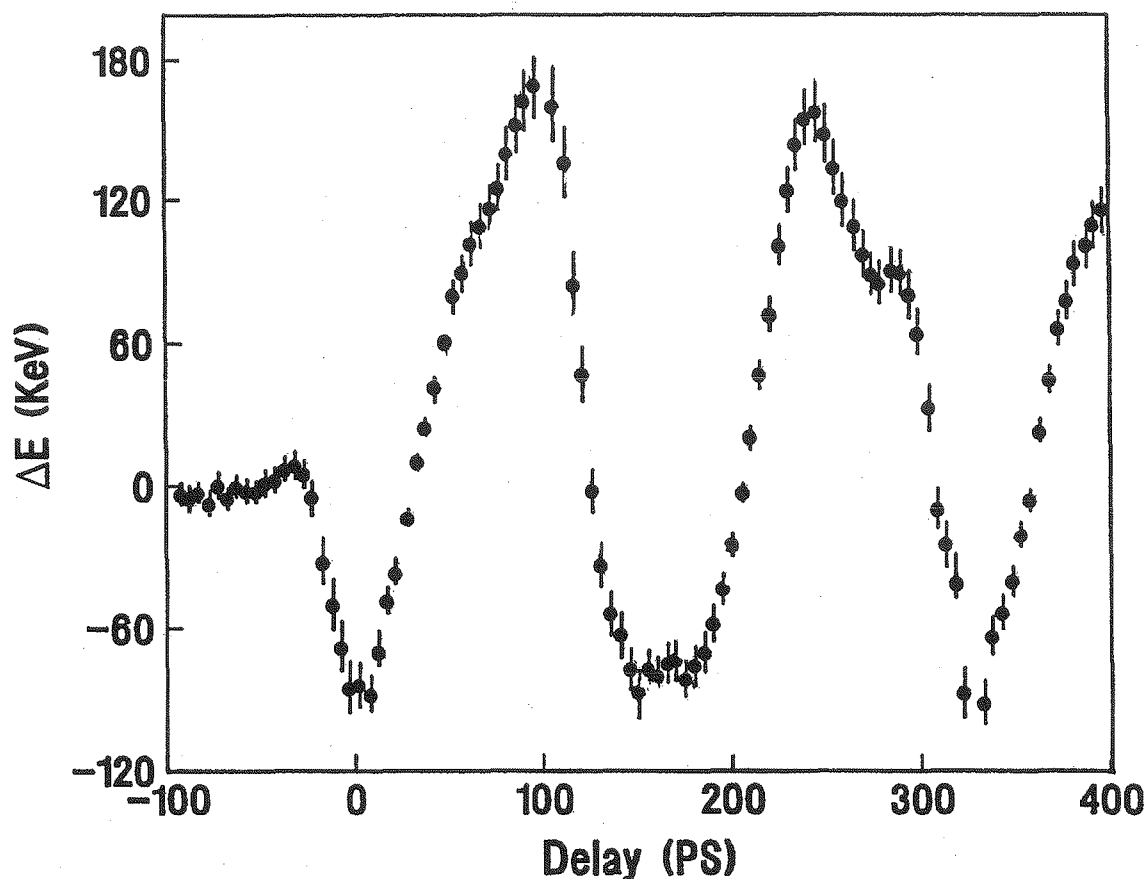


Figure 4-6. Wakefield measurement by Simpson et al. [13]

from its neighboring cavities. Minute differences in radii and length cause each cavity to have slightly different resonant frequencies. The use of several cavities of slightly different resonant frequencies is used in the design of klystrons for broadband amplification. The summation of different resonant frequencies causes Simpson's experiment to have a broader frequency response than, for example, a single cavity.

A fundamental difference between the experimental data and the theoretical data is an evanescence caused by the use of a practical excitation source. Figure 4-7 illustrates this effect. The definition of beam impedance requires the excitation source to be an impulse of current, which is physically impossible. The use of a Gaussian (Eq. 2-6) or a time-limited-cosine-squared (Eq. 2-8) source to excite the cavity are closer to realistic geometries in use for many particle accelerators. This will cause the "measured" beam impedance to artificially decrease with increasing frequency, thereby lowering the excitation of the higher-order modes.

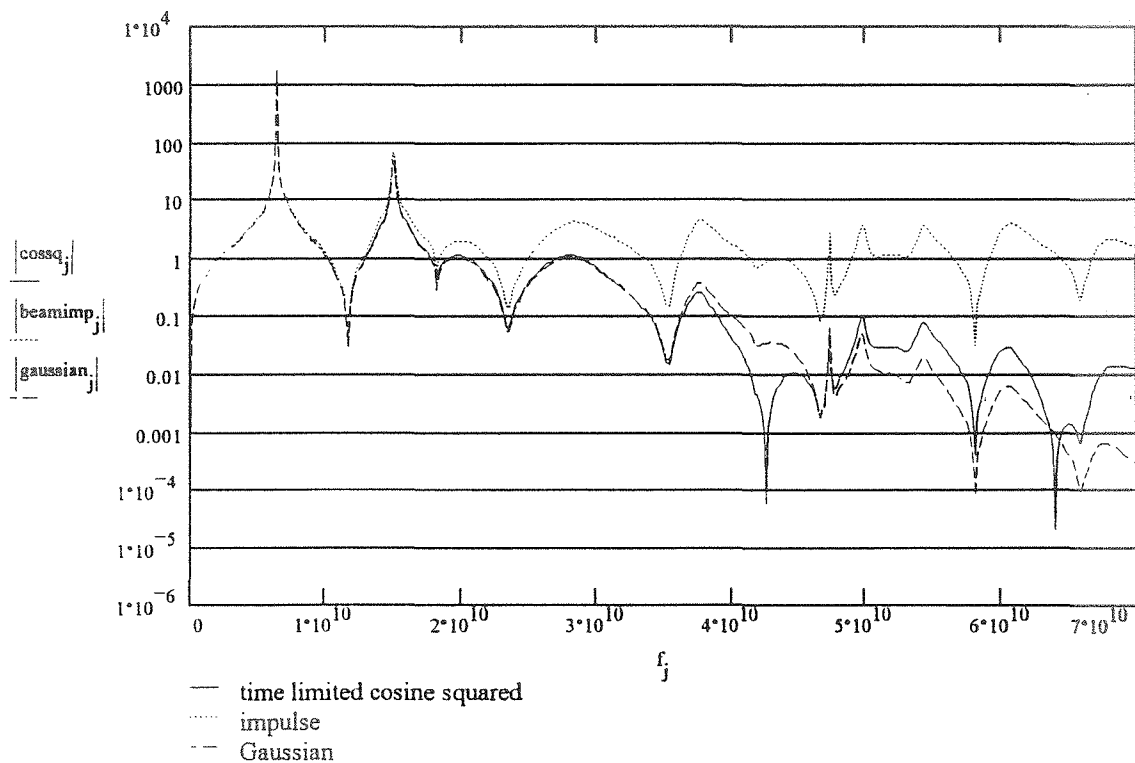


Figure 4-7. Impedances (Ω) caused by different source distributions versus frequency (Hz).

Simulation of a Gaussian witness bunch interacting with a Gaussian beam impedance did not show any appreciable change in the time domain data. There is, however, a stronger evanescence in the frequency domain for the Gaussian source-Gaussian witness than in an impulse source-Gaussian witness. The low-frequency cavity modes were excited equally from the Gaussian source-impulse witness as the impulse source-Gaussian witness calculation of the wakefield. The net effect was that the high-frequency decay did not play a significant role in the time domain results when either a practical driving source and/or a practical witness source was considered.

D. Conclusions

The analytical tools presented in this chapter provide a method to adequately solve the integral equation in Eq. 1-12 with the use of Eq. 4-7. It is important to know the first cutoff frequency of the beampipe as well as the frequency of the first pillbox cavity mode in order to appraise whether or not it is necessary to modify the resulting beam impedance data. The modification method presented in this chapter applies only to pillbox modes which are coupled strongly to the particle beam. It is necessary to consider practical current source geometries in the analysis since an impulse of current has infinite bandwidth.

V. Stretched Wire Analysis

A. Theoretical Solution

i. Introduction

The solution to the problem in Fig. 1-9 with a center conductor of radius $r=r_0$ is estimated using the same complex Fourier series techniques used to solve the open beampipe geometry and current sources described in Ch. IV. Since the general method of solving Eq. 1-12 is identical to the charged particle beam, a discussion of the differences and changes in estimating the solution of Eq. 1-12 for the geometry with the center conductor will be presented.

ii. Change in Pipe Kernel Definition and Cavity Coupling

The first difference between the stretched wire measurement and a physical beam is the obvious change in geometry and boundary conditions caused by the introduction of the center conductor. Mathematically, this changes the definition of the pipe kernel in the analysis of Eq. 1-12, and Eq. 1-8 must be used for the pipe kernel rather than Eq. 1-6. The additional coefficient terms of Eq. 1-8 (the α_s in Eq. 1-9) describe the differences in coupling between the cavity modes of either the open beampipe or the center conductor beampipe. Physically, adding the center conductor has three fundamental effects. First, it allows energy to couple into and out of the cavity via the TEM pipe mode. Secondly, it shifts the cutoff frequencies of the TM

waveguide modes of the beampipe. Finally, the addition of the center conductor introduces a set of coefficients in the definition of the center conductor pipe kernel in Eq. 1-8. Each coefficient in Eq. 1-9 dictates a different level of coupling from the waveguide pipe modes to the cavity modes than what was observed in the open beampipe. In fact, the coupling from the beampipe to each cavity mode is stronger for the center conductor beampipe than for the open beampipe.

Estimating the coupling coefficients for asymptotic calculations was performed by first finding the cutoff frequencies of the center conductor beampipe from the equation

$$J_0(i_s) Y_0(i_s \frac{r_o}{a}) = J_0(i_s \frac{r_o}{a}) Y_0(i_s).$$

When $i_s \gg 1$ and $i_s \frac{r_o}{a} \gg 1$, the asymptotic forms of the Bessel functions were used to find

$$i_s \approx \frac{s\pi}{1 - \frac{r_o}{a}}, \quad \alpha_s = \frac{J_0^2(i_s \frac{r_o}{a})}{J_0^2(i_s \frac{r_o}{a}) - J_0^2(i_s)} \approx \frac{1}{1 - \frac{r_o}{a} \frac{\cos^2\left(\frac{s\pi a}{a - r_o} - \frac{\pi}{4}\right)}{\cos^2\left(\frac{s\pi r_o}{a - r_o} - \frac{\pi}{4}\right)}}.$$

As $s \rightarrow \infty$, α_s does not have a formal limit. To estimate the truncation error of the center conductor pipe matrix requires an estimate of α_s for large s . The propagating pipe modes and the lowest order evanescent modes make the largest contribution to the pipe kernel. Examining α_s for large s shows that a bound for α_s exists and is

$$\alpha_s \leq \alpha = \frac{a}{a-r_o}.$$

Replacing α_s by α introduces an error to the estimate of the pipe kernel. To reduce the error from the introduction of α , the point of truncation for the series in Eqs. D-1 and D-2 must be sufficiently high such that the leftover series uses the estimate of α . The truncated sum must be much greater than the leftover sum.

Figure 5-1 is a plot of α_s versus s for a 50- Ω coaxial beampipe. Calculating the limiting value α for the 50- Ω geometry shows $\alpha=1.769$. For a 50- Ω geometry, the first 15-20 α_s fail the assumption that $i_s \frac{r_o}{a} \gg 1$ and these first 15-20 terms must be

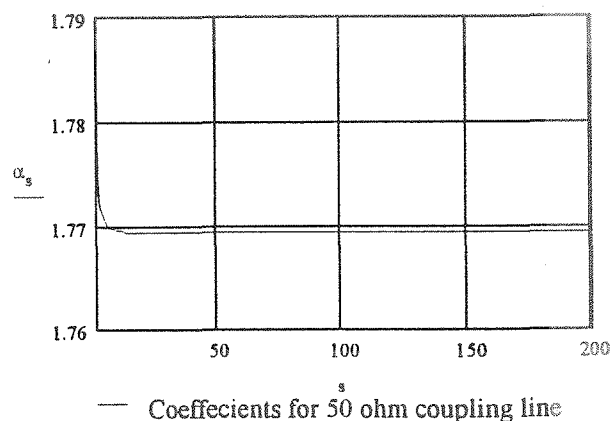


Figure 5-1. Plot of the actual α_s for a 50- Ω coupling line.

individually calculated in the summation of the pipe kernel. Consequently, the *minimum* point of truncation must be large enough such that α_s remains relatively constant. The final 180 α_s , however, appear to converge to the bound. The error in the estimate of the truncation error is therefore minimized by choosing the point of truncation to be: 1) large enough to include several evanescent modes and all propagating modes and 2) large enough such that the α_s has settled to a point where an estimate of it can be adequately made.

iii. Addition of a Loss Mechanism and Data Modification

The presence of the wire may reduce the numerics of the computation because the wire adds an effective loss mechanism to all of the cavity modes. The loss mechanism is a consequence of the TEM pipe mode and its ability to carry stored energy out of otherwise loss-less cavity modes. A loss mechanism was discussed in Ch. IV, Figs. 4-1 and 4-2, as a numerical necessity for the existence of a causal inverse Fourier transform of the beam impedance. Since the computed data will be causal, the additional loss mechanism reduces the post-computation work and therefore does not require the changes that the computation depicted in Fig. 4-1 suffers. No computational savings will be experienced, however, between the open beampipe and the center conductor beampipe if the resonant frequency of the first cavity mode occurs

above the cutoff frequency of the open beampipe.

iv. Change in Definition of the Beam Impedance

An obvious difference with the presence of the wire is the required change in the definition of beam impedance. The mere existence of the wire on axis requires the wakefield to identically vanish. It has been proposed that the fields are only locally disturbed by the presence of the wire and a similar wakefield-type quantity may be defined by shifting the location of the definition for the wakefield to a position off-axis. Arbitrarily, it is chosen to define a new path of integration for defining the wakefield from Fig. 1-1 to a path along the wall of the beampipe. The modified definition for the beam impedance from Appendix A is then

$$\tilde{Z}_{beam}(\omega) \triangleq -\frac{1}{Q} \int_0^g E_z(r=a, z, \omega) e^{ikz} dz,$$

where $E_z(r=a, z, \omega)$ is computed with a complex Fourier series along the interval $\{0 \leq z \leq g\}$. Examination of the limits of the integration in this new definition implies that the contribution to the wakefield exists only at the specific location of the cavity. The inability for both the propagating and evanescent pipe modes to interact with the beam outside of $\{0 \leq z \leq g\}$ is a nonphysical assumption. It has been shown with stretched wire measurements that the

evanescent pipe fields of a cavity mode contain significant energy. The evanescent pipe fields can be, to first order, taken into consideration by allowing the unperturbed cavity fields to evanesce into the pipe [14]. The effect of propagating pipe modes and its coupling to cavity modes are not as easily estimated, and general conclusions cannot be easily drawn.

This definition for the impedance is not necessarily useful. The presence of the wire shorts out the accelerating electric field. The off-axis electric field is thereby attenuated several orders of magnitude. This term will not be used or discussed in the remaining portions of this dissertation.

v. Beampipe Cutoff Frequency Change

Adding the center conductor has the effect of changing the TM cutoff frequencies of the beampipe. Note that the cutoff frequencies for each TM pipe mode always increase with the addition of a center conductor. If the addition of the center conductor causes the cutoff frequency of a beampipe mode to shift such that a dominant cavity mode couples energy into an evanescent pipe mode rather than a propagating pipe mode, then the stretched wire measurement may show an artificially higher Q than what is witnessed with a charged particle beam. In the same way, the addition of the center conductor can cause the Q of cavity modes to appear

artificially low if the cavity modes occur in a frequency regime where the TEM pipe mode is dominant over the lowest cutoff frequency beampipe mode. Figure 5-2 is a contrived example which demonstrates this phenomenon. Figure 5-2 is a relative plot of the magnitude of the open beampipe kernel (Eq. 1-6) and the center conductor beampipe kernel (Eq. 1-8) for a particular value of $z=z'=0$. The cavity energy storage is an integration of the electric and magnetic fields in the region $\{0 \leq r \leq b; 0 \leq z \leq g\}$ and has units of joules. In Fig. 5-2 it is assumed that the shift in cavity resonant frequency caused by the introduction of the wire is negligible with respect to the shift in the first TM cutoff frequency of the

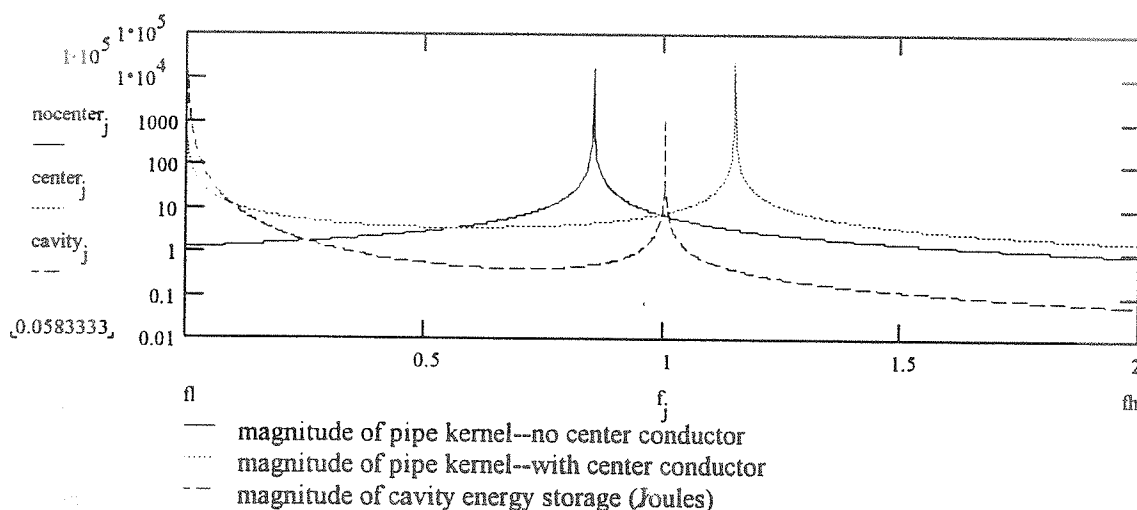


Figure 5-2. Relative plot of the pipe kernels (dimensionless) and cavity energy storage (joules) versus normalized frequency. Note the shift in cutoff frequency between the open beampipe and the beampipe with the center conductor. Between the cutoff frequencies is a cavity mode, which would have an artificially higher Q with the center wire present.

beampipe. The strong peaks in the cavity plot of Fig. 5-2 show that the cavity stores energy in its modes at both $\omega=0$ and $\omega=2\pi$. Each of the pipe kernels has the property that a particular pipe mode behaves strongly in the frequencies near the vicinity of the cutoff frequency of each pipe mode. Additionally, each propagating pipe mode decays as

$$\frac{c}{\omega a} \left(1 - \left(\frac{j_s c}{2\omega a} \right)^2 \right)$$

with $\omega \gg \omega_{cutoff}$ for each respective pipe mode s . Since the first dominant mode for the center conductor pipe kernel is the TEM mode and its cutoff frequency is $\omega_0 = i_0 = 0$, the effective coupling of the TEM pipe mode is inversely proportional to frequency. The dominant propagating pipe mode for a particular bandwidth B contributes the most to the loss mechanism for all the cavity modes with resonances contained within B . Therefore, if frequency is high enough such that the TEM mode is sufficiently decayed out of the pipe kernel, and if a TM pipe mode exists whose cutoff frequency passes through a cavity mode by the introduction of the wire, then the cavity mode will have an artificially higher Q in the presence of the wire.

vi. *Example of a Relationship between SWM Impedance to Beam Impedance*

a. *Introduction*

The use of network analyzers to perform stretched wire measurements requires a formula to relate the scattering parameters back to the beam impedance Z_{beam} . The derivation of this relationship requires the following assumptions:

- $k \triangleq \frac{\omega}{c}$, a frequently used definition for wave number used throughout this dissertation.
- $ka \ll 1$, an implication that the frequency of interest is far below the first TM cutoff frequency of the beampipe. This assumption allows an additional assumption that $E_z(r=a, z) \approx E_z(r=0, z)$.
- $kg \ll 1$, an assumption that the z dependence of $E_z(r, z)$ is constant, i.e., $E_z(r=a, z) = \gamma_0$, where γ_0 is a constant. The requirement of $kg \ll 1$ may be relaxed, for example, by demanding that

$$E_z(r=a, z) \triangleq f(z) = \sum_{l=-1}^{l=1} \gamma_l e^{i \frac{2l\pi z}{g}}.$$

Using this assumption, however, changes the proceeding results. Allowing higher dimensions in the estimate of $E_z(r, z)$ allow a more rigorous and broadband estimate of both circuit and beam impedances.

- impulse source distribution defined in Eq. 2-3.

- $k(b-a) \rightarrow 0$ assumes that the size of the discontinuity is small with respect to a wavelength.

Since $E_z(r, z)$ is assumed to be a constant function of z , Eq. 4-7 changes into a simple linear equation of one equation and one unknown. The $\underline{\Theta}$ and $\underline{\Xi}$ matrices each become a 1×1 matrix whose only elements are $\theta_{0,0}$ and $\xi_{0,0}$, respectively. The $\underline{\Phi}$ vector contains one element, ϕ_0 . The constants of the linear equation, namely $\xi_{0,0}(\omega)$ and $\phi_0(\omega)$, need to be calculated once since their definitions do not change between the analysis of the SWM and the real charged particle beam. The $\theta_{0,0}$ changes between the two scenarios and needs to be recomputed with each respective analysis.

b. Calculation of Z_{beam}

Applying the definition of Eq. 4-6 to the impulse current source in Eq. 2-3 reveals

$$\phi_0 = \frac{2\pi Z_o}{ika} \int_0^g \frac{I_o}{2\pi a} e^{-ikz} dz = \frac{Z_o I_o}{k^2 a^2} (e^{-ikg} - 1).$$

Since $kg \ll 1$, ϕ_0 may be estimated as $\phi_0 \approx \frac{-iZ_o I_o g}{ka^2}$ since $e^{-ikg} \approx 1 - ikg$ for $kg \ll 1$. The formulae for calculating the elements of the matrix equation are found in Appendix D.

Using Eq. 4-4 to find $\xi_{0,0}$ is rather involved since one is required to find all of the cavity modes and their respective normalizations. At low frequency, however, the dominant mode of the cavity kernel is the DC mode described

in Eq. 3-3. The effect of the DC mode on $\xi_{0,0}$ is

$$\xi_{0,0DC} = 4\pi^2 \int_0^g \int_0^g dx dy \frac{1}{2\pi g \ln(\frac{b}{a}) k^2 a^2} = \frac{2\pi g}{\ln(\frac{b}{a}) k^2 a^2}.$$

The truncation error of $\xi_{0,0}$ is therefore the sum of all the cavity modes besides $\xi_{0,0DC}$. The truncation is a sum which is a real constant that can be calculated. Define the truncation error ξ_T as

$$\xi_{0,0} \triangleq \xi_{0,0DC} + \xi_T.$$

The terms $\xi_{0,0DC}$ and ϕ_0 are both singular as $k \rightarrow 0$. For low frequencies note that $\xi_{0,0DC} \gg \xi_T$.

Calculating $\theta_{0,0}$ using Eq. 4-3 with the pipe kernel of Eq. 1-6 shows that $\theta_{0,0}$ is bounded for $k \rightarrow 0$. Comparing $\theta_{0,0}$ to $\xi_{0,0}$ reveals $\theta_{0,0} \ll \xi_{0,0}$. This implies that the dominant factors in the linear equation are the DC cavity mode and the excitation source. Inserting $\theta_{0,0}$, $\xi_{0,0}$, and ϕ_0 into Eq. 4-7 identifies the linear relationship

$$(\theta_{0,0} + \xi_{0,0DC} + \xi_T) \gamma_0 = \phi_0.$$

Solving for γ_0 results in

$$\gamma_0 = \frac{-ikZ_o I_o \ln(\frac{b}{a})}{2\pi \left(1 + \frac{k^2 a^2 \ln(\frac{b}{a})}{2\pi g} [\theta_{0,0} + \xi_T] \right)}.$$

Inserting the definition of γ_0 into the normalized definition of beam impedance in Eq. A-1 results in

$$Z_{beam}(\omega) = -\frac{1}{Q} \int_0^g E_z e^{ikz} dz = -\frac{1}{Q} \int_0^g \gamma_0 e^{ikz} dz \approx -\gamma_0 \frac{g}{Q}$$

$$\therefore Z_{beam}(\omega) = \frac{ikZ_o \ln\left(\frac{b}{a}\right) g}{2\pi \left(1 + \frac{k^2 a^2 \ln\left(\frac{b}{a}\right)}{2\pi g} [\theta_{0,0} + \xi_{0,0T}]\right)} \approx \frac{i\omega Z_o \ln\left(\frac{b}{a}\right) g}{2\pi c}.$$

This equation is correct to first order and shows the well-known result that the beam impedance of a change in beampipe diameter equates to magnetic energy storage [15].

c. Calculation of S_{21}

The mathematics of the center conductor beampipe requires an additional term (from the additional TEM mode) that the open beampipe did not possess. Using Eq. 1-8 in the definition of $\theta_{0,0}$ reveals

$$\theta_{0,0} = \frac{2\pi i}{a} \sum_{s=0}^{\infty} \frac{\alpha_s}{\tilde{b}_s} \int_0^g \int_0^g dx dy e^{-i \frac{\tilde{b}_s}{a} |x-y|}$$

$$= \frac{2\pi \alpha_0}{k^2 a^2} \left[-2ig + \frac{2(1-e^{-ikg})}{k} \right] + \theta_{0,0T}.$$

The second term in this expression, $\theta_{0,0T}$, is a real number and has a numerically predictable relationship to the $\theta_{0,0}$ calculated for the open beampipe. The first term, however, is the result of the TEM contribution to E_z . Expanding this expression for $kg \approx 0$ shows that there is *no* TEM contribution to E_z .

Inserting the results of the calculation of $\theta_{0,0}$, $\xi_{0,0}$, and ϕ_0 into Eq. 4-7 produces

$$(\theta_{0,0T} + \xi_{0,0DC} + \xi_{0,0T}) \gamma_0 = \phi_0.$$

Solving for γ_0 results in

$$\gamma_0 = \frac{-ikZ_o I_o \ln(\frac{b}{a})}{2\pi \left(1 + \frac{k^2 a^2 \ln(\frac{b}{a})}{2\pi g} [\theta_{0,0T} + \xi_{0,0T}] \right)}.$$

The transmission coefficient is found by substituting the γ_0 into Eq. 1-10. This results in a calculated transmission coefficient of

$$s_{21}(\omega) = 1 - \frac{i\omega g \ln(\frac{b}{a})}{2c \ln(\frac{a}{r_o}) \left(1 + \frac{k^2 a^2 \ln(\frac{b}{a})}{2\pi g} [\theta_{0,0T} + \xi_{0,0T}] \right)},$$

corresponding to a lumped circuit element of²

$$Z_{\text{circuit}}(\omega) \approx \frac{ikZ_o \ln\left(\frac{b}{a}\right)g}{2\pi}.$$

Again, this equation is correct to first order. If frequency is low enough such that the higher-order terms can be neglected, the TEM circuit impedance converges to the beam impedance exactly. The presence of the magnetostatic cavity mode allows the circuit impedance to converge to the beam impedance. The low frequency circuit model derived in this section is different than the high frequency model presented in Fig. 1-7 in Ch. I.C. The difference in each respective model represents different frequency assumptions.

vii. Summary

The presence of the wire can dictate a strong cavity mode evanescence caused by the addition of the TEM loss mechanism. Ironically, the presence of the wire may also cause the measured Q of a particular cavity mode to increase if the shift in pipe cutoff frequency changes about the cavity resonant frequency and the TEM mode can be neglected. The introduction of the wire requires a new pipe kernel in Eq. 1-12. The wire may decrease the post-computation work since the wire introduces an effective loss mechanism to all cavity modes.

² A description of the formulation for calculating the circuit impedance from S_{21} is found in Appendix E.

B. Center Conductor Cutoff Effects

It is important to know the effect of the relative size of the center conductor on the cutoff frequency of the beampipe in order to know how the solution of the open beampipe compares to the solution of the stretched wire measurement.

In the following work, it is assumed that the region of interest only includes the first cutoff frequency. The method is general enough such that it can be applied to any of the cutoff frequencies and the results are likewise similar.

$$J_0(j_1) = 0, \quad J_0(i_1) Y_0(i_1 \frac{r_o}{a}) = J_0(i_1 \frac{r_o}{a}) Y_0(i_1), \quad (5-1)$$

Consider the two transcendental equations which respectively determine the set of cutoff frequencies for the case of the open beampipe and the stretched wire measurement: where

$$k_{cutoff} = \frac{j_1}{a} \quad k_{cutoff} = \frac{i_1}{a}.$$

Assuming that $\frac{r_o}{a} \ll 1$, substitute the small argument form of the Bessel functions [16] into the formulae of Eq. 5-1 and take the Taylor series expansion of both $J_0(x)$ and $Y_0(x)$ about the point $x=j_1$. After several algebraic manipulations, it is

possible to show that

$$\frac{\Delta j}{j_1} \triangleq \frac{j_1 - j_1}{j_1}$$

varies directly (for $\frac{r_o}{a} \ll 1$) with the ratio

$$\frac{\Delta j}{j_1} \propto \frac{1}{\ln\left(\frac{r_o}{a}\right)}.$$

Figure 5-3 is a linear scale plot of $\frac{\Delta j}{j_1}$ versus the ratio of center conductor radius (r_o) to the beampipe outer conductor radius (a). Near $\frac{r_o}{a} \approx 0$ in Fig. 5-3 it appears as if $\frac{\Delta j}{j_1}$ approaches a constant value of $\frac{\Delta j}{j_1} \approx 0.15$. Changing the axis to a logarithmic scale in Fig. 5-4 allows a more detailed

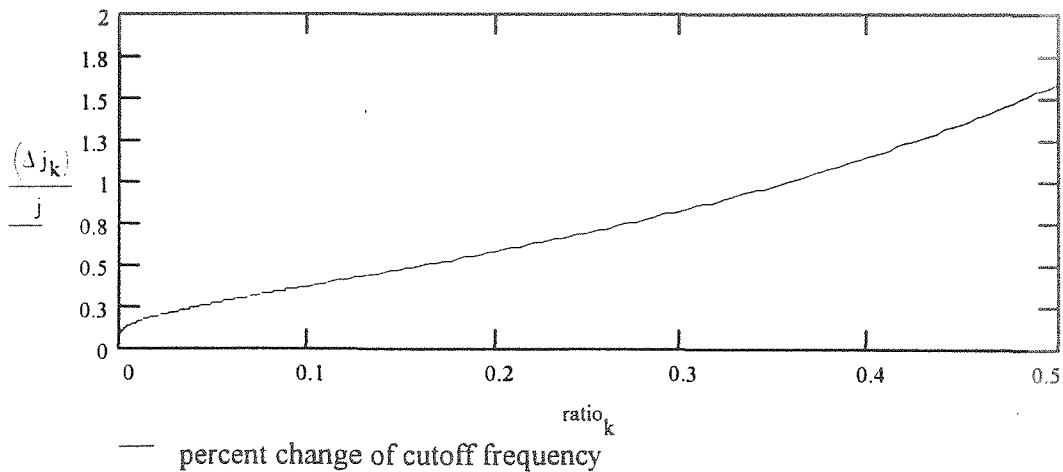


Figure 5-3. Graph depicting the dependence of the percent change in cutoff frequency on the ratio of center conductor to outer conductor.

view of the origin and the dependence of $\frac{\Delta j}{j_1}$ for small $\frac{r_o}{a}$. Mathematically, it is clear that in the limit of $\frac{r_o}{a} \rightarrow 0$ that $\frac{\Delta j}{j_1} \rightarrow 0$. It is not practical for $\frac{r_o}{a} \rightarrow 0$ and perhaps only a ratio of $\frac{r_o}{a} \approx 0.05$ is in practice achievable. Using the limiting ratio $\frac{r_o}{a} = 0.05$ causes a frequency shift $\frac{\Delta j}{j_1}$ of about 25%. Shifting the cutoff frequency of the beampipe by 25% is significant and this effect *must* be included in the final interpretation of the results.

Most network analyzers and microwave measurements are made using 50- Ω coaxial TEM transmission lines. From Fig. 5-3, using a 50- Ω TEM coaxial geometry (i.e., $\frac{r_o}{a} \approx \frac{1}{2.3}$) requires the cutoff frequency of the first TM mode to be almost *doubled* from that of an open beampipe. Figure 5-2 showed that shifting the cutoff frequencies of the beampipe changed the measured Q's of cavity modes. It is clear that care must be exercised and measurements must be scrutinized

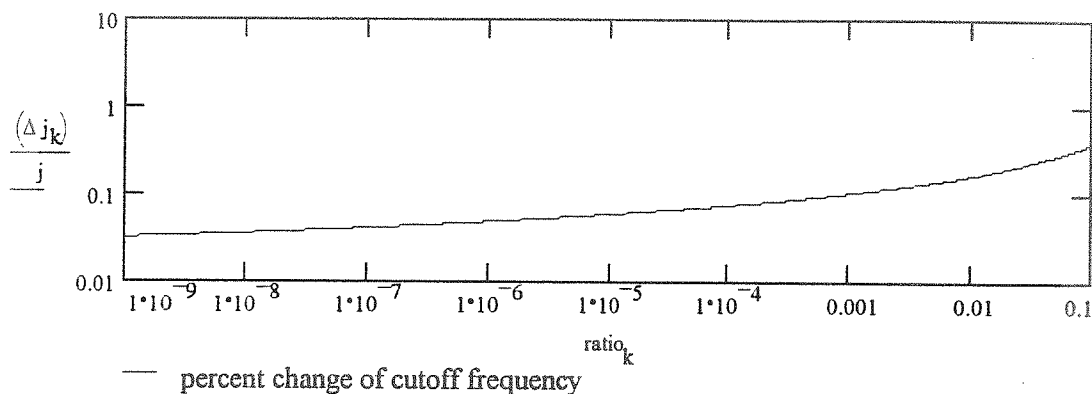


Figure 5-4. Logarithmic scale of the graph depicted in Fig. 5-3.

when using the center conductor to simulate a beam of relativistic charge.

C. Measurement Data

i. Introduction

The goal of this dissertation is to compare the stretched wire measurement with a real beam measurement. The real beam measurement is described in Ch. IV and was performed by Simpson et al. The stretched wire measurement was designed around the parameters Simpson used in his experiment:

- $a=0.63$ cm / 0.248 in.
- $b=1.95$ cm / 0.768 in.
- $g=0.32$ cm / 0.125 in.
- $r_o=0.274$ cm / 0.108 in. $\approx 50\text{-}\Omega$ reference line.

A reference line, shown in Fig. 5-5, was constructed out of eight individual and interlocking pieces of brass to fit the geometry dictated by Simpson's experiment. Two linear tapered sections change the geometry from the $50\text{-}\Omega$ cables connected to the ports on the network analyzer to a $50\text{-}\Omega$ air dielectric coaxial transmission line. The outer diameter of the straight section is equal to Simpson's beampipe diameter. Commercially purchased SMA connectors were soldered to the machined center conductor to make stretched wire measurements.

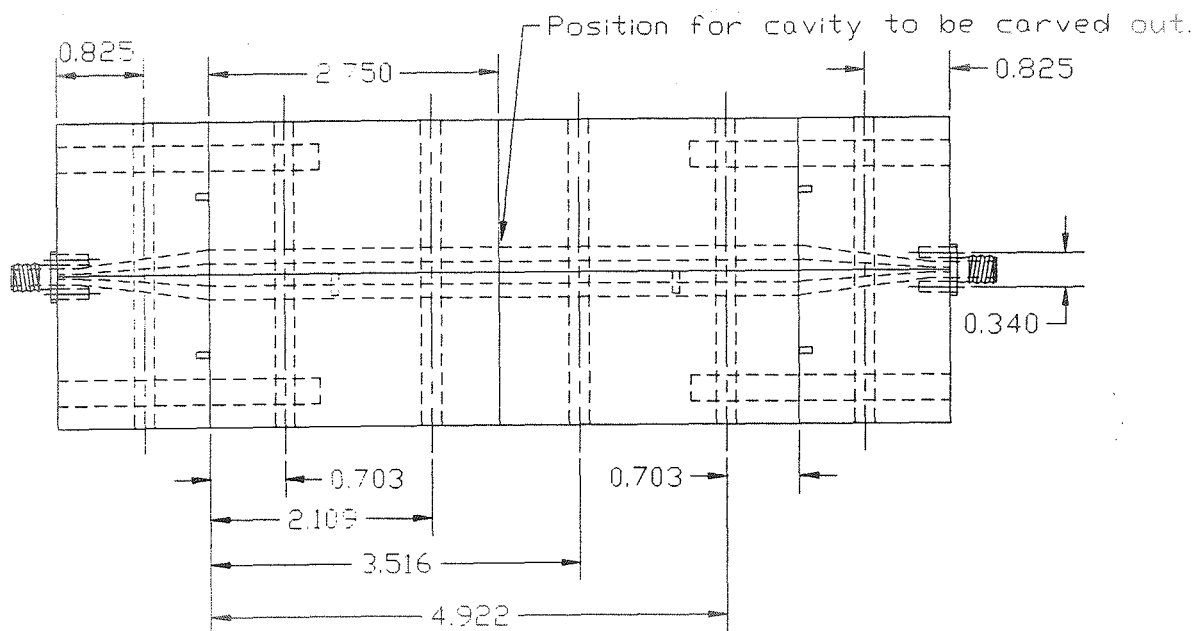


Figure 5-5. CAD drawing for the 50- Ω reference line used in the stretched wire measurement. All dimensions are in inches.

The measurement results will be presented by first showing the frequency domain results from a network analyzer and then by showing the results of a short impulse that was fed into the cavity and comparing it with the frequency domain measurements. Interpretations of the different measurement techniques on the beam impedance and wakefield will finally be presented.

ii. Network Analyzer Measurement Considerations

a. Reference Measurement

Before the cavity was carved into the structure, the scattering (s) parameters were measured to establish the reference measurement [17]. The stretched wire measurement was performed with a 20-GHz HP 8510C network analyzer.

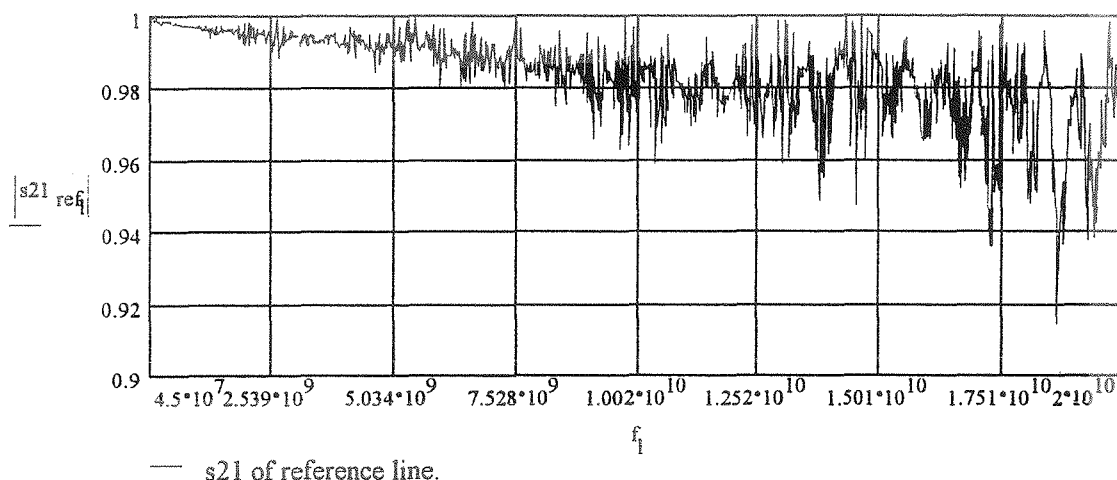


Figure 5-6. Linear magnitude plot of S_{21} versus frequency (Hz). The periodic ripple is a result of a resonance caused by mismatches of the connectors with the physical length of the reference line in Fig. 5-5.

Figure 5-6 is a linear scale plot of the magnitude of the transmission (S_{21}) for the reference line. This plot shows relatively good transmission for the entire bandwidth of the measurement, having a minimum transmission $|S_{21}|=0.915$ at 18 GHz. The periodic ripple in the measurement is caused by a resonance between the physical length of the reference section and the dielectric mismatch at the interface between each connector and the tapered sections of the reference line. The ripple is easily observed in the measurement of reflection (S_{11}) depicted on a logarithmic scale in Fig. 5-7.

In the frequency range of 8.5-15.5 GHz small "noise-like" resonances can be seen. Several phenomena cause these small resonances including:

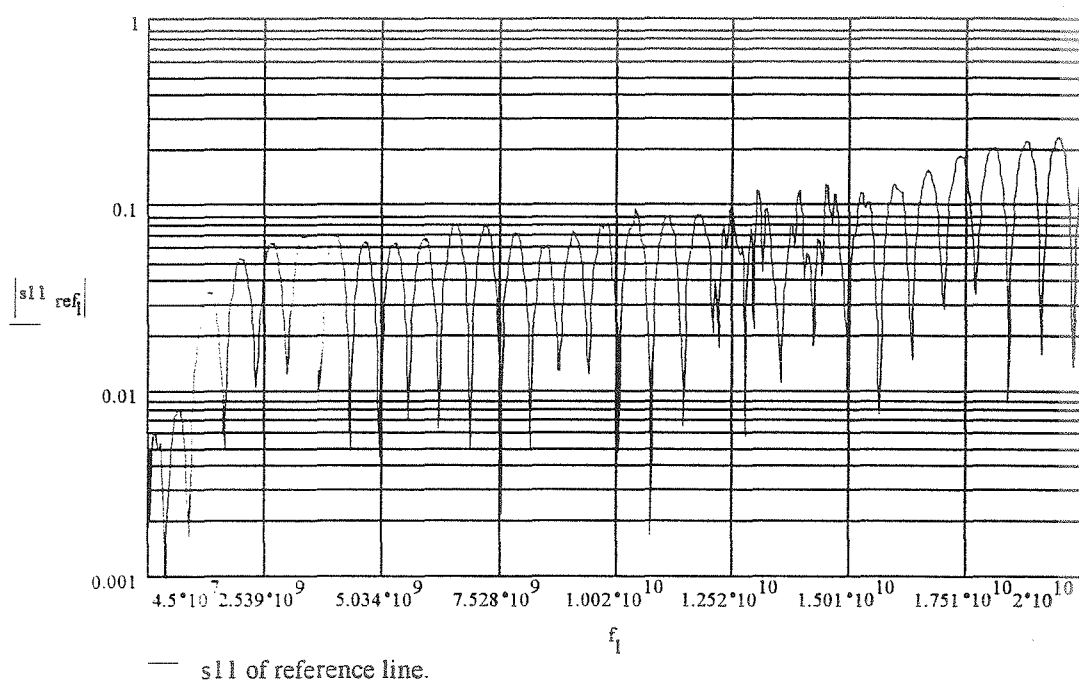


Figure 5-7. A plot of the log magnitude of the reflection coefficient (s_{11}) versus frequency (Hz). The periodic ripple is caused by mismatches between the SMA connectors in Fig. 5-4 and the tapered section of the reference line.

- The two linear tapered matching sections are not the same physical length, and each of these lengths produces resonances at slightly different frequencies. This may cause the measurement to appear "noisy" when in fact multiple resonances appear close together.
- The tapered sections of the center conductor and the outer housing have radial geometrical differences. These include small angular differences in the tapered sections between the center conductor and housing as well as non-smooth interfaces between the tapered sections and straight sections. These reflections

resonate with the electrical length of the tapered section.

Tiny pieces of solder embedded in the connectors, poor solder joints, and structural anomalies were detected by calculating the inverse Fourier transform of the reflection coefficients. The inverse Fourier transforms of $|s_{11}(\omega)|$ and $|s_{22}(\omega)|$ are

plotted in Figs. 5-8a and 5-8b to verify that the reflections from each port of the reference line is of the same magnitude.

The two large peaks in the impulse response of Figs. 5-8a and 5-8b represent the reflections caused by mismatches from each connector. The small ripples at time $t=0.33$ ns in Fig. 5-8a and time $t=1.33$ ns in Fig. 5-8b are caused by a

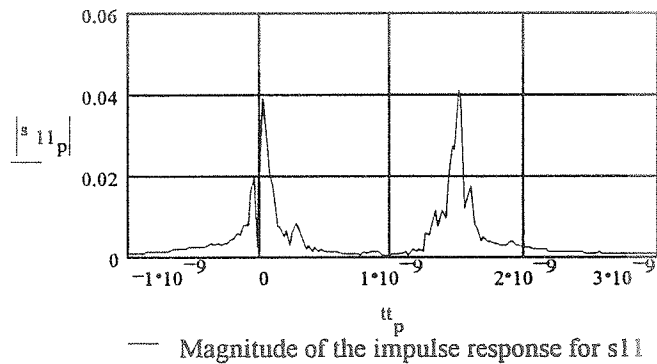


Figure 5-8a. Magnitude of the impulse response for s_{11} versus time (s). The two sharp peaks are reflections caused by each connector.

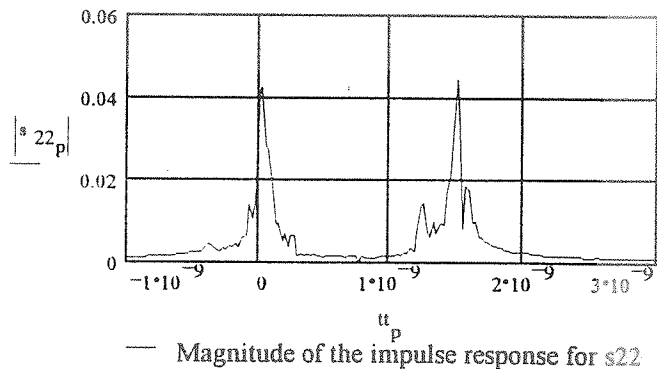


Figure 5-8b. Magnitude of the impulse response for s_{22} versus time (s). Note the similarity in the magnitude of the reflections with Fig. 5-8a.

small machining imperfection between the tapered and straight sections on port 1.

b. Pillbox Cavity Measurement and Prediction

After the reference data were collected, the reference line was disassembled, and a single-cell pillbox cavity was carved into the housing. A drawing of the new geometry is depicted in Fig. 5-9. The frequency domain measurements of $|S_{11}|$ and $|S_{21}|$ are shown in Figs. 5-10 and 5-11, respectively. A close correspondence is seen between the predicted and measured reflection and transmission. The periodic ripple observed in Fig. 5-7 is again observed in Fig. 5-10, but only for frequencies away from the sharp resonances depicted in the $|S_{21}|$ measurement in Fig. 5-11. The phase of the prediction and reflection again showed excellent correspondence.

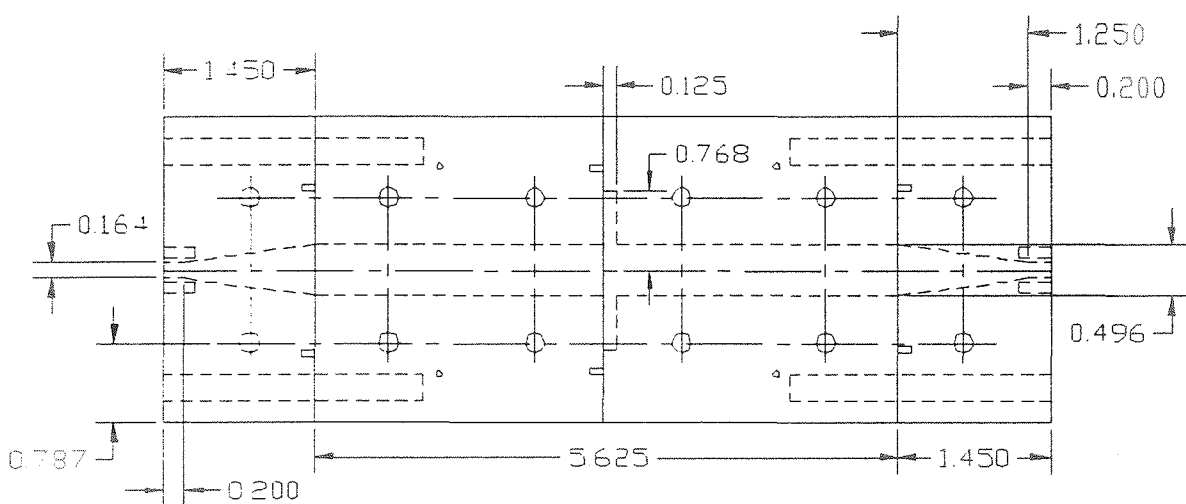


Figure 5-9. Reference line with a small pillbox cavity carved into the midsection.

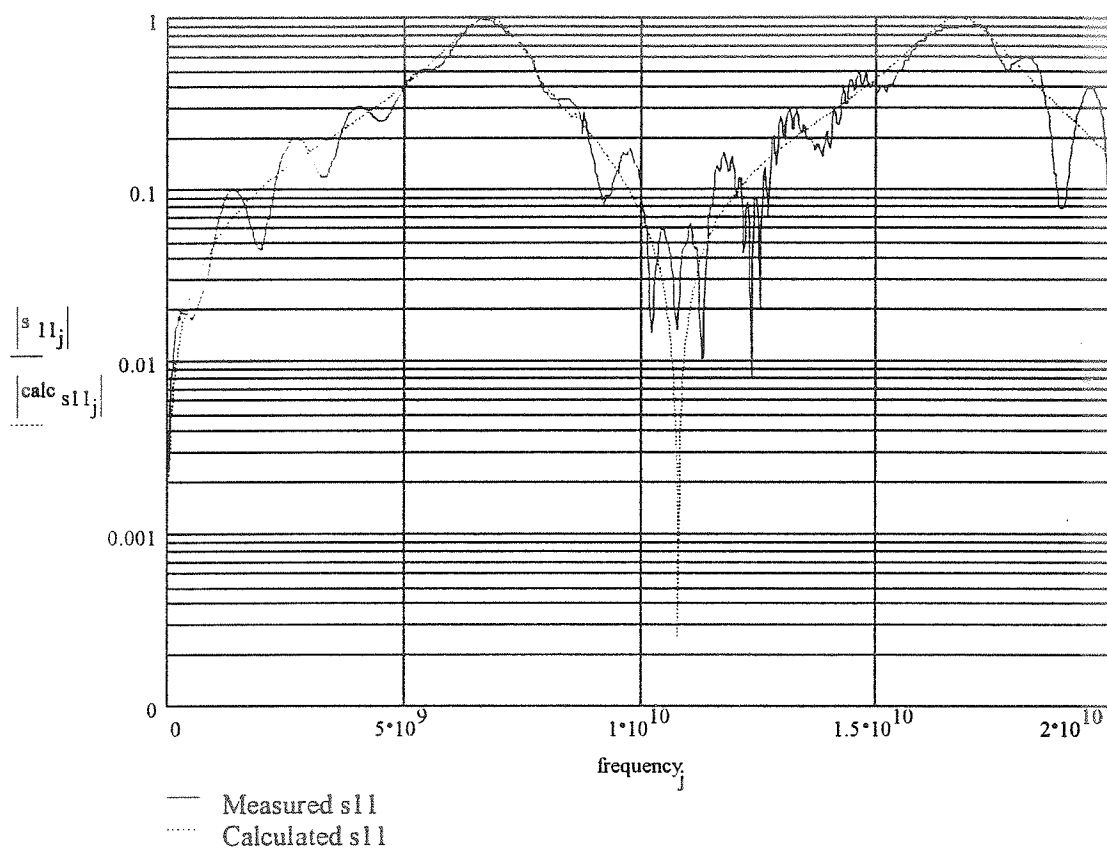


Figure 5-10. Plot of measured and calculated reflection versus frequency (Hz). The ripples in the measurement were caused by residual mismatches and discontinuities in the matching network.

The $TM_{0,1,0}$ resonant frequency for a coaxial cavity with inner and outer radii at 0.274 cm and 1.95 cm, respectively, is 8.6 GHz, whereas the $TM_{0,1,0}$ resonant frequency for a pillbox cavity of radius 1.95 cm is 5.88 GHz. The sharp decreases in transmission in the measurement of Fig. 5-11 correspond therefore to the parallel resonance of the net capacitance from the series cavity impedance with the inductive coupling mechanism shown in Fig. 1-7.

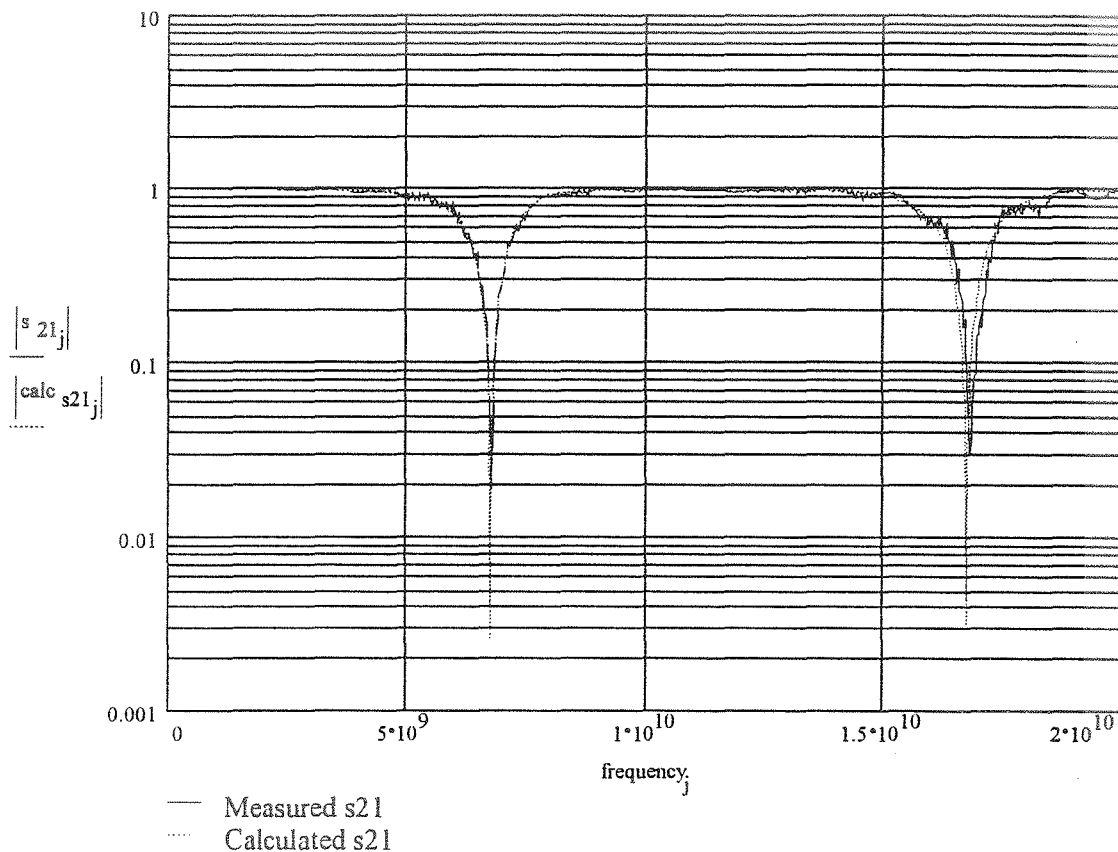


Figure 5-11. Plot of measured and calculated transmission S_{21} versus frequency (Hz).

iii. Time Domain Measurements and Results

The impulse response of the cavity structure in Fig. 5-9 was measured using the experimental setup in Fig. 5-12. A personal computer was used to record the measurement data from the HP 54120B 50-GHz sampling oscilloscope. Channel 1 on the HP 4124A produces a train of long rise-time step functions at a low repetition rate (50 kHz) which trigger a Picosecond Pulse Lab (PSPL) 4015 pulse generator. The PSPL 4015 produces a short rise-time step function. The short

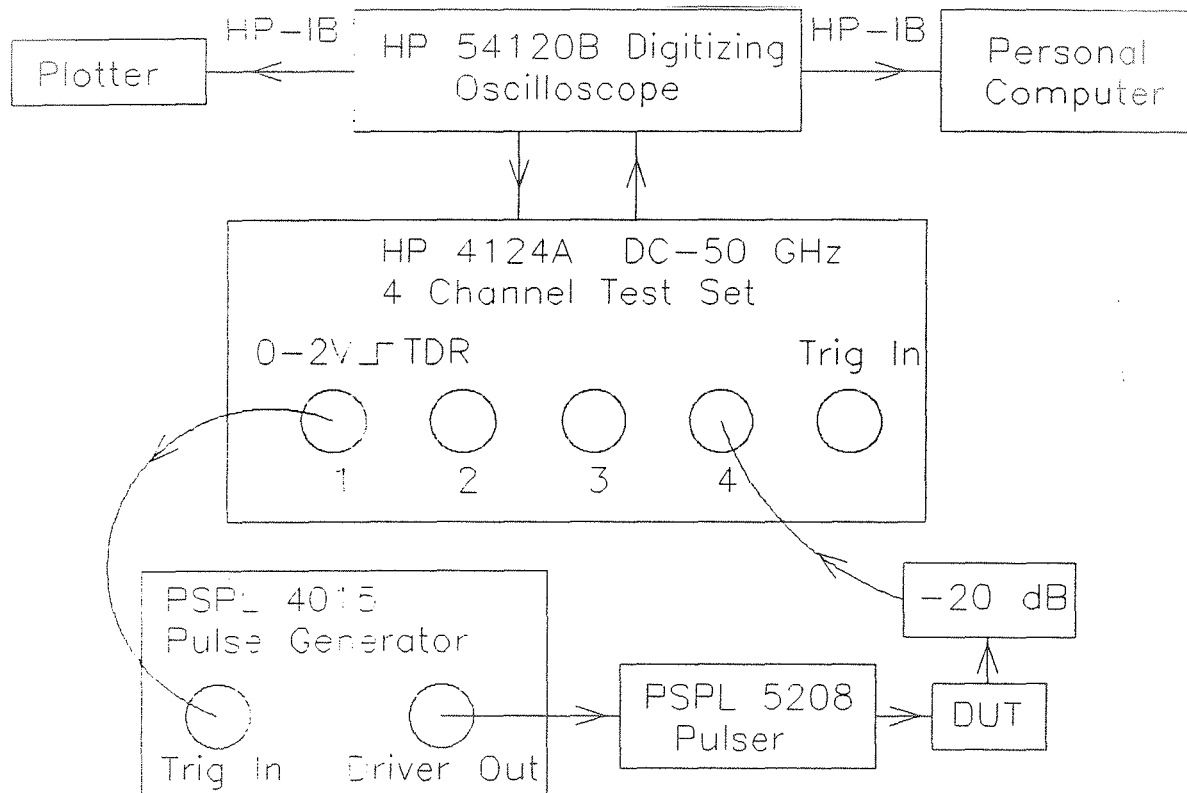


Figure 5-12. Schematic for the time domain impulse response stretched wire measurement for a general DUT.

step is fed into a matched passive waveforming network (PSPL 5208) which functions as a differentiator. Since the input to the PSPL 5208 is a step function, the output of the PSPL 5208 is an impulse. A plot of the measured impulse is shown in Fig. 5-13.

When the impulse from Fig. 5-13 is fed into the cavity of Fig. 5-9, the physical length of the structure causes the resulting waveform to be shifted in time. The cavity response to the pulse of Fig. 5-13 is time shifted 632 ps

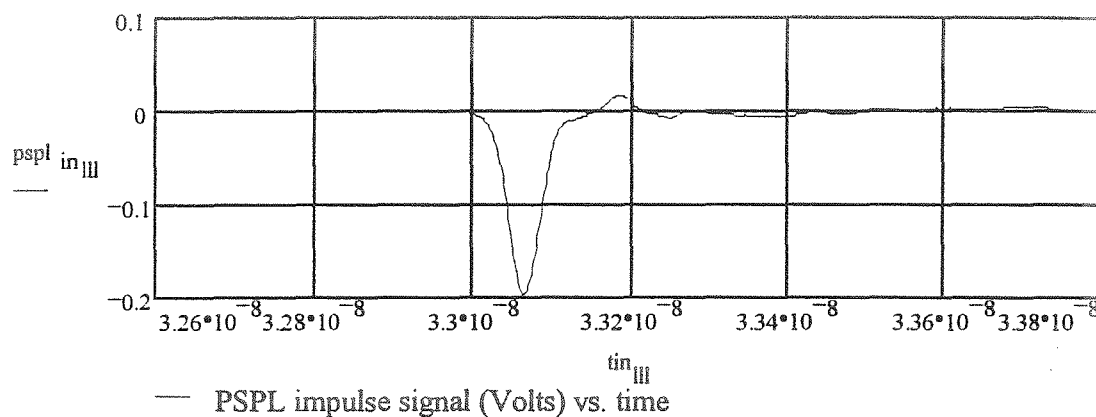


Figure 5-13. Output waveform from the PSPL 5208 waveforming network (V) versus time (s).

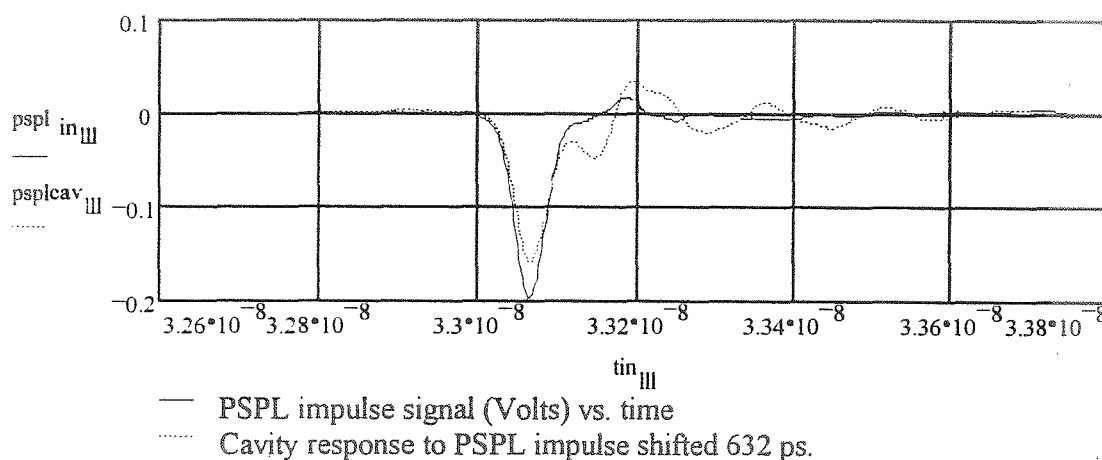


Figure 5-14. Shifted cavity response (V) to the impulse of Fig. 5-13 versus time (s).

resulting in Fig. 5-14. The time shift of the cavity response in Fig. 5-14 allows the plot of both the pulse and cavity response to be conveniently displayed on one graph.

To find the transmission of the cavity, it is necessary to find the transfer function of the cavity. This was performed by first analyzing the problem in the frequency

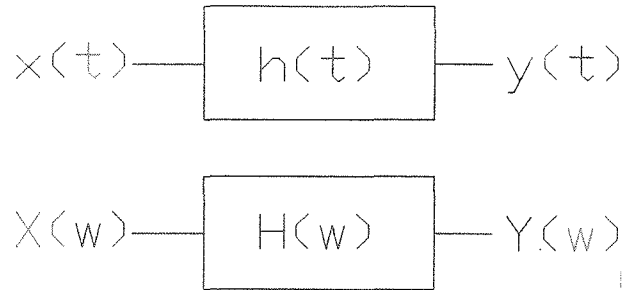


Figure 5-15. General system parameters.

domain and then making the assumption that the cavity network is a linear system. First, the spectrum of the time-domain input signal in Fig. 5-13 was calculated. Next the spectrum of the time-domain cavity response, $Y(\omega)$ in Fig. 5-15, to the input was calculated. Examination of the system and signals in Fig. 5-15 leads to the following definitions:

$x(t) \triangleq$ input signal

$y(t) \triangleq$ output response due to excitation $x(t)$

$h(t) \triangleq$ system transfer function

$$\therefore H(\omega) = \frac{Y(\omega)}{X(\omega)}.$$

The time-domain data was assumed to be zero when the measurement data had the same order of magnitude as the noise floor of the sampling scope [18]. The spectra of the input signal $X(\omega)$ and the output signal $Y(\omega)$ are presented in Fig. 5-16.

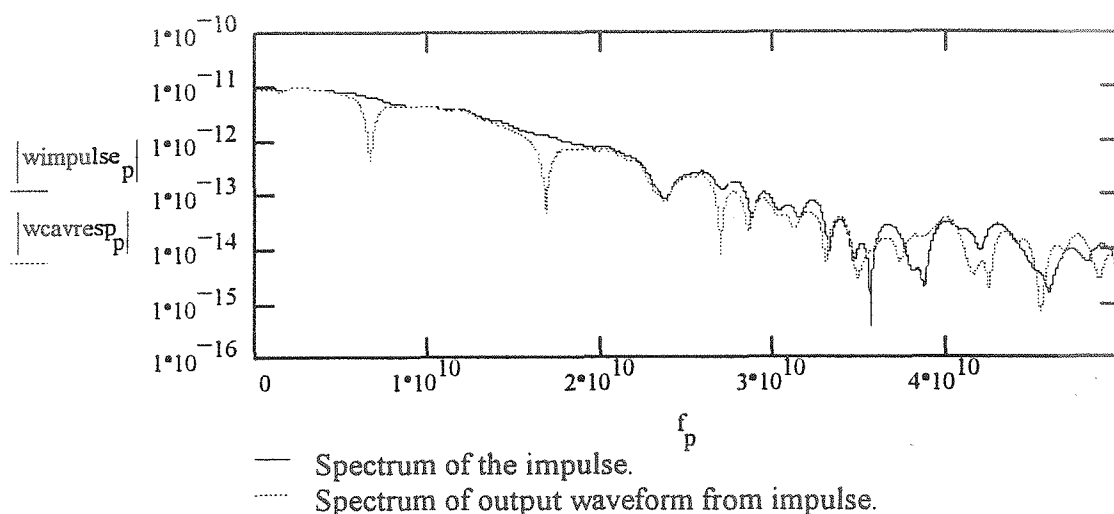


Figure 5-16. Input spectrum to the cavity and the output spectrum from the cavity due to the input to the cavity.

Using Parseval's Fourier transform relationship

$$\int_{-\infty}^{\infty} |x(t)|^2 dt = \frac{1}{2\pi} \int_{-\infty}^{\infty} |X(\omega)|^2 d\omega,$$

the frequency-domain response was truncated at 28 GHz. The spectrum of the transmission $|H(\omega)|$ for the cavity is plotted in Fig. 5-17. Since the network analyzer that made the frequency-domain measurement had an upper limit on its frequency synthesizer, a comparison of the calculated frequency response to the frequency-domain network analyzer measurement was desired. The results of this comparison are plotted in Figs. 5-18 and 5-19. Figure 5-18 is a frequency-domain plot comparing the network analyzer measurement of

$|s_{21}|$ to the Fourier transformed time-domain measurement of transmission. Figure 5-19 is a plot showing the similarity of the inverse Fourier transform of $s_{21}(\omega)$ and the calculated impulse response from the time-domain measurement of the cavity structure. These results show that the stretched wire measurement can be treated as a linear measurement.

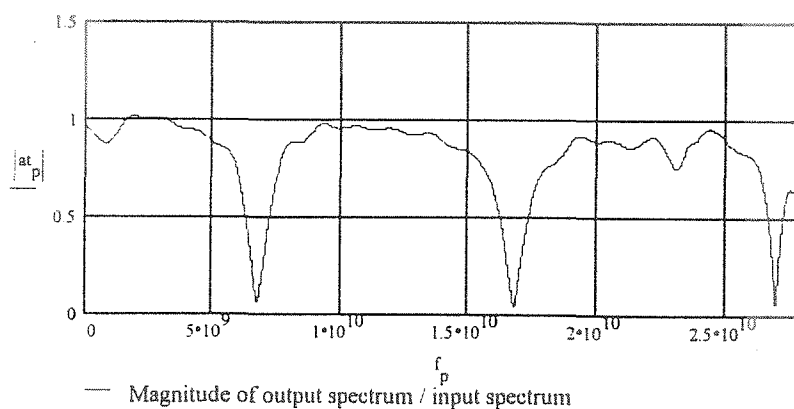


Figure 5-17. Magnitude of impulse response of cavity structure from time-domain data.

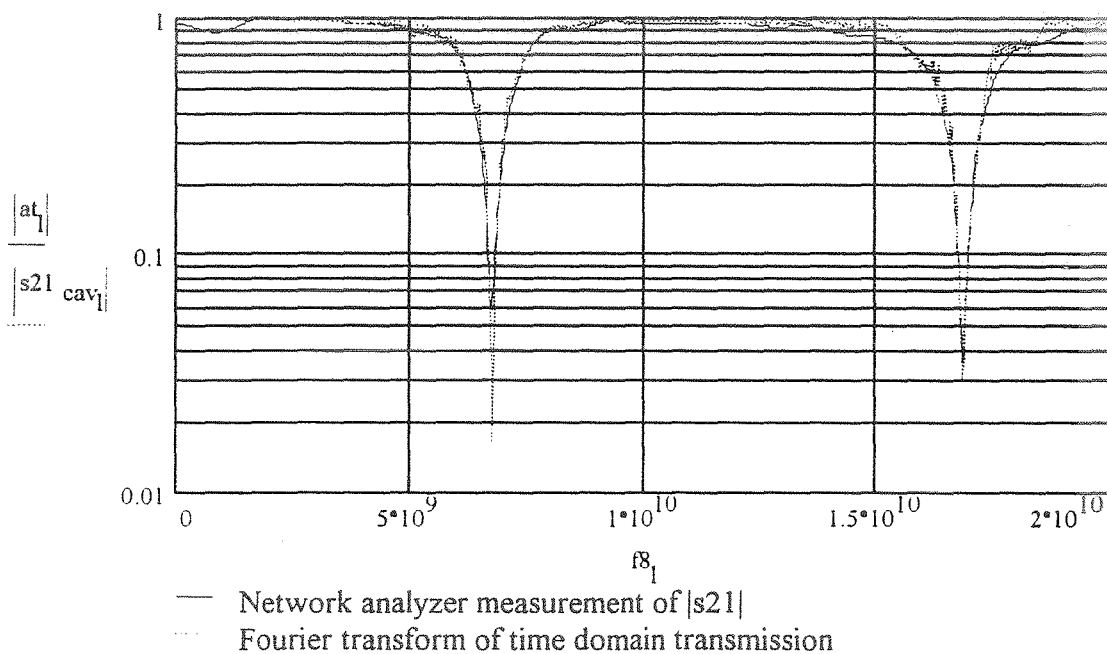


Figure 5-18. Comparative plot between the frequency response from the analysis of the time-domain measurement to the network analyzer measurement.

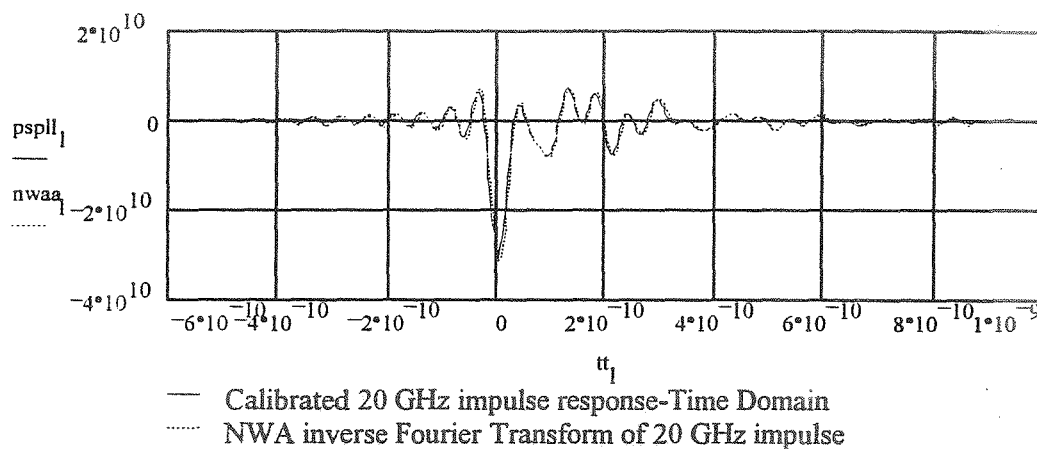


Figure 5-19. Impulse response to the cavity network (V) compared to the inverse Fourier transform of the S_{21} data from the network analyzer versus time (s).

iv. *Comparison of Beam Impedance to Circuit Impedance*

a. *Introduction*

The general equation used to find the lumped circuit impedance from the scattering parameters measured with the reference and cavity stretched wire measurements is

$$Z(\omega) = 2R_{o\text{reference}} \left(\frac{S_{21\text{ref}}(\omega) - S_{21\text{DUT}}(\omega)}{S_{21\text{DUT}}(\omega) S_{21\text{ref}}(\omega)} \right). \quad (5-2)$$

Using this equation reduces the effects of the connectors, length of the reference line, and other various non-idealities of the practical measurement. The quantity $R_{o\text{reference}}$ is the characteristic impedance of the straight section of the reference line.

b. *50-Ω Reference Line Measurement of Circuit Impedance*

A plot of the measured circuit impedance, using Eq. 5-2 with the data in Figs. 5-10 and 5-11, versus frequency is shown in Figs. 5-20 and 5-21. Figure 5-22 is a plot of the predicted beam impedance from the impulse source of Fig. 4-7 and a plot of the SWM circuit impedance. A strong similarity exists in the SWM technique to predict the beam impedance in the frequencies away from the cavity resonances. The 50-Ω SWM measures a circuit impedance of the same magnitude and shifted in frequency from the estimate of beam impedance.

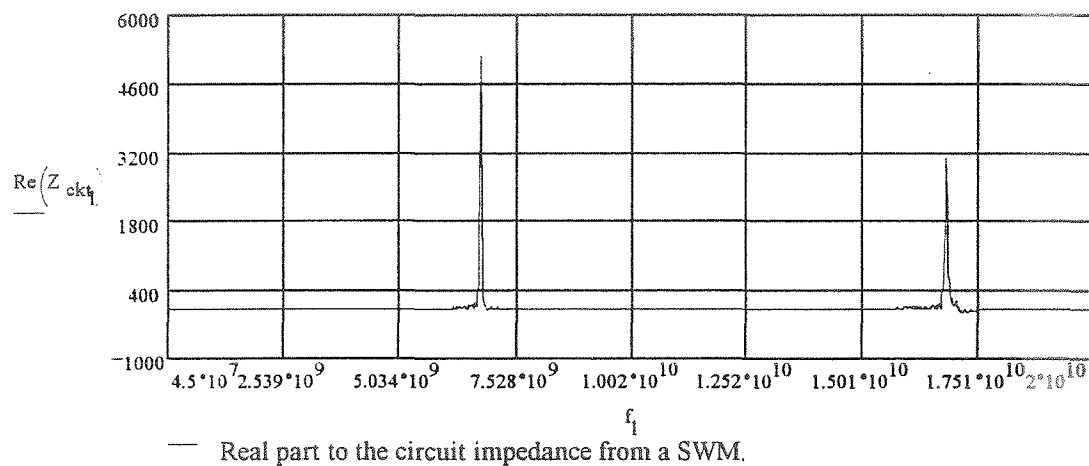


Figure 5-20. Plot of the real part of the circuit impedance (Ω) from a SWM versus frequency (Hz).

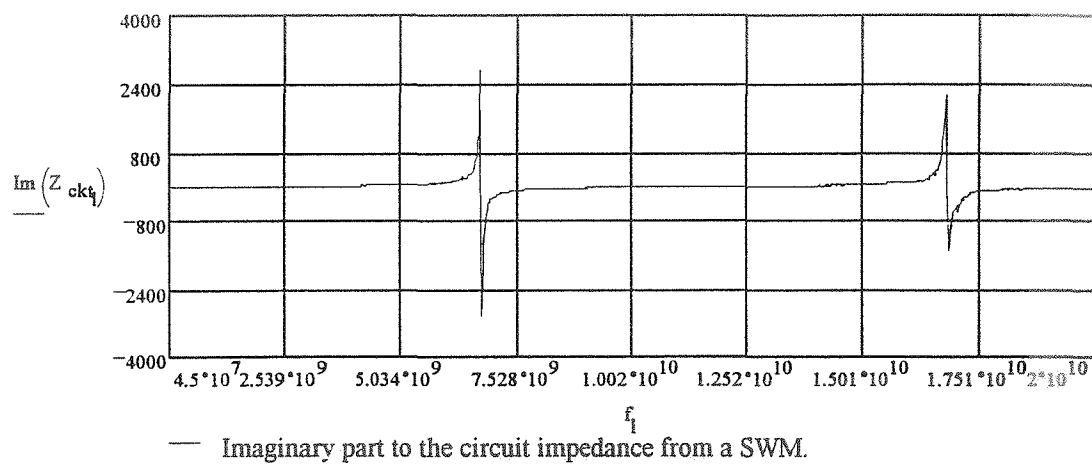


Figure 5-21. Plot of the imaginary part of the circuit impedance (Ω) from a 50- Ω SWM versus frequency (Hz).

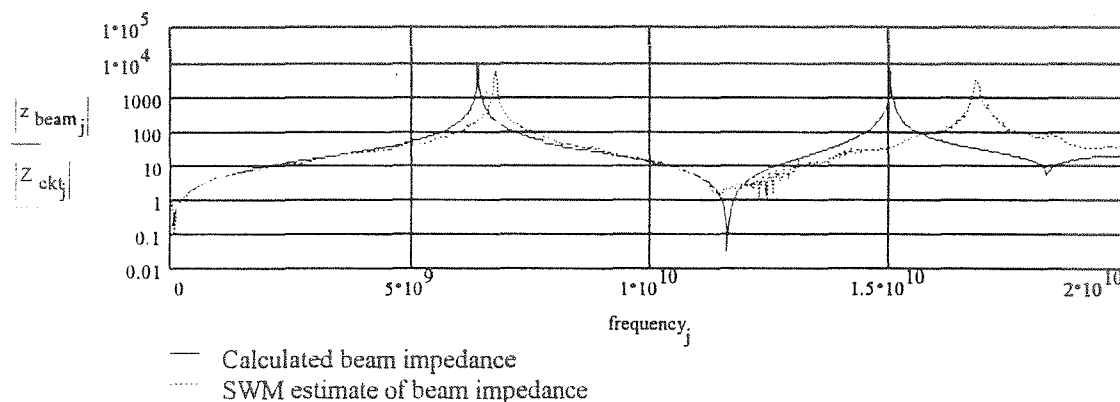


Figure 5-22. A plot of the predicted beam impedance (Ω) and the 50- Ω SWM estimate of beam impedance (Ω) versus frequency (Hz).

c. Use of Non-50- Ω Reference Lines

Sands and Rees originally postulated the use of a small center conductor to measure beam impedance. Two non-50- Ω reference line geometries, one at 84 Ω and the other at 42 Ω , were measured to find their effects on the measured circuit impedances and compared to the estimated beam impedance. The outer diameter structure remained the same as shown in Fig. 5-5 while the center conductor geometry was changed to accommodate the different impedance reference lines. The center conductor tapered sections of Fig. 5-5 remained linear to match wave impedances from the impedance of the reference line to the 50- Ω cables from the network analyzer. The length of the tapered sections, therefore, caused strong reflections for frequencies below ~ 2 GHz.

First, the 42- Ω reference line was measured. The results of the $|S_{21}|$ cavity and reference measurements are plotted in Fig. 5-23. Using the relationship in Eq. 5-2, the measured circuit impedance is plotted in Fig. 5-24 together with the measured circuit impedance from the 50- Ω line data presented in Fig. 5-11. As expected, the larger center conductor of the 42- Ω reference line shifts the frequencies of the cavity resonances higher, but is essentially the same as the 50- Ω reference line measurements in frequency regimes away from the pillbox and coaxial cavity resonant frequencies.

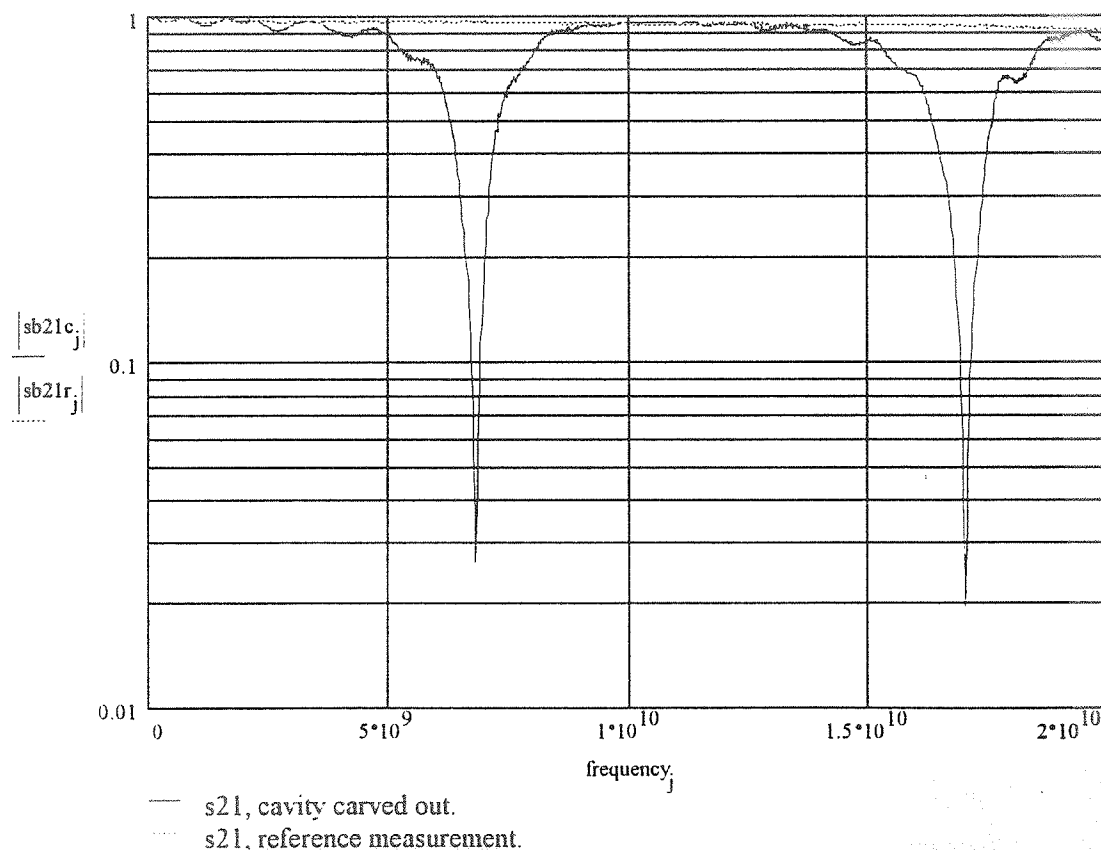


Figure 5-23. Reference and SWM with a 42- Ω coupling line for the pillbox cavity versus frequency (Hz).

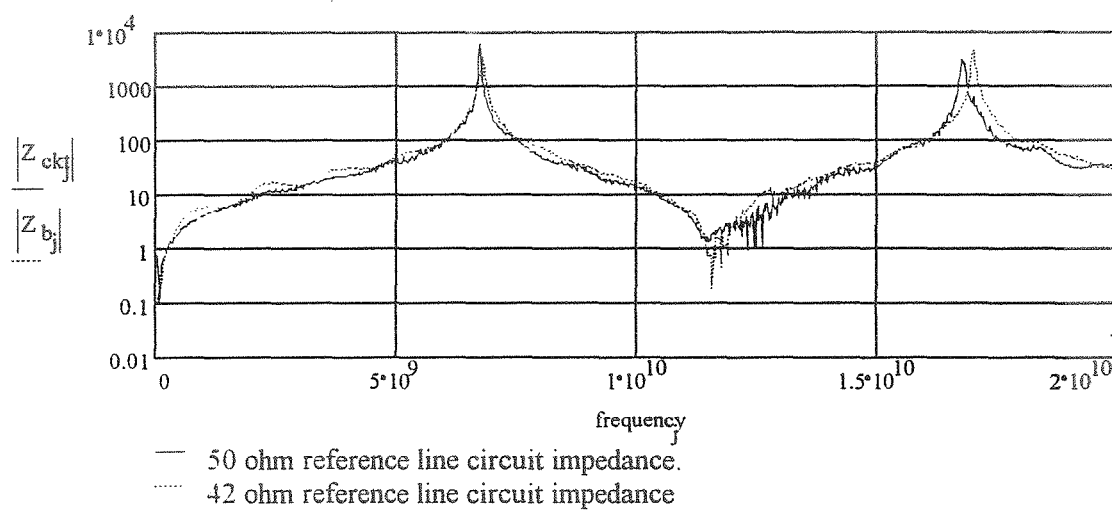


Figure 5-24. Measured circuit impedances (Ω) for the 50- Ω and 42- Ω reference lines versus frequency (Hz).

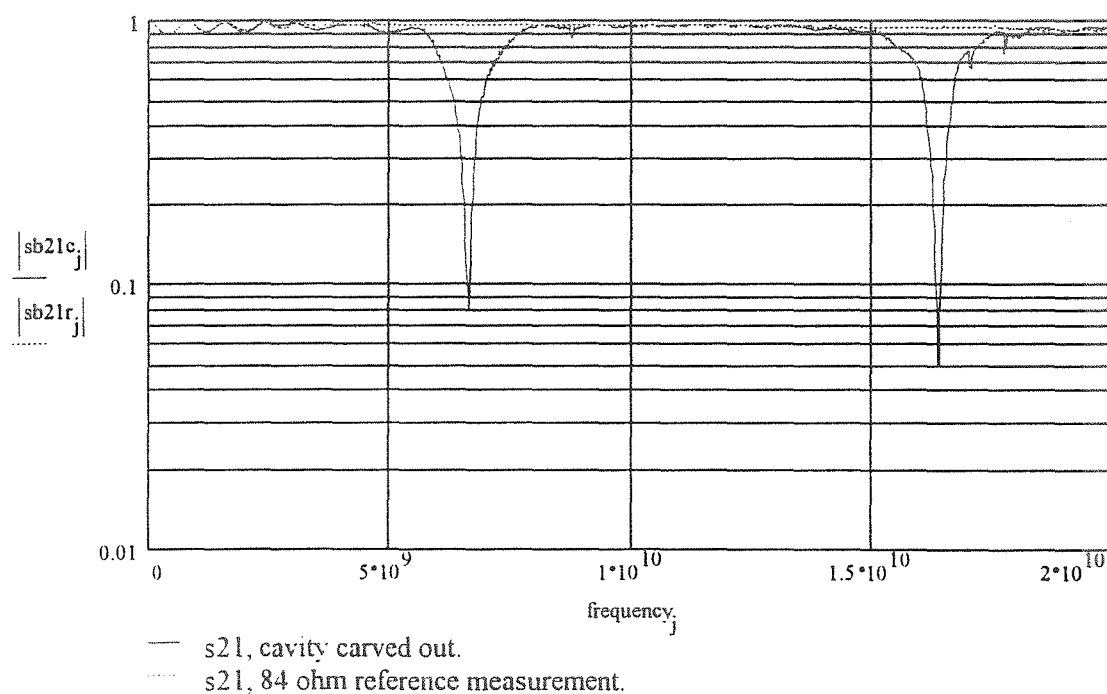


Figure 5-25. Reference and SWM measurements for an 84- Ω reference line versus frequency (Hz).

Next, the 84- Ω line was measured. This particular reference line had stronger reflections than the 42- Ω line. The $|S_{21}|$ reference and cavity stretched wire measurements are plotted in Fig. 5-25. The circuit impedance was calculated from the $|S_{21}|$ measurement using Eq. 5-2 and are plotted in Fig. 5-26 together with the circuit impedance measured with the 50- Ω reference line. As was expected, the cavity mode shift due to the presence of the 84- Ω reference wire was not as pronounced as was observed in the 50- Ω case.

A plot of the measured circuit impedance and predicted beam impedance is shown in Fig. 5-27. The measured cavity resonant frequency corresponds more closely with the 84- Ω reference line to the predicted beam impedance resonant

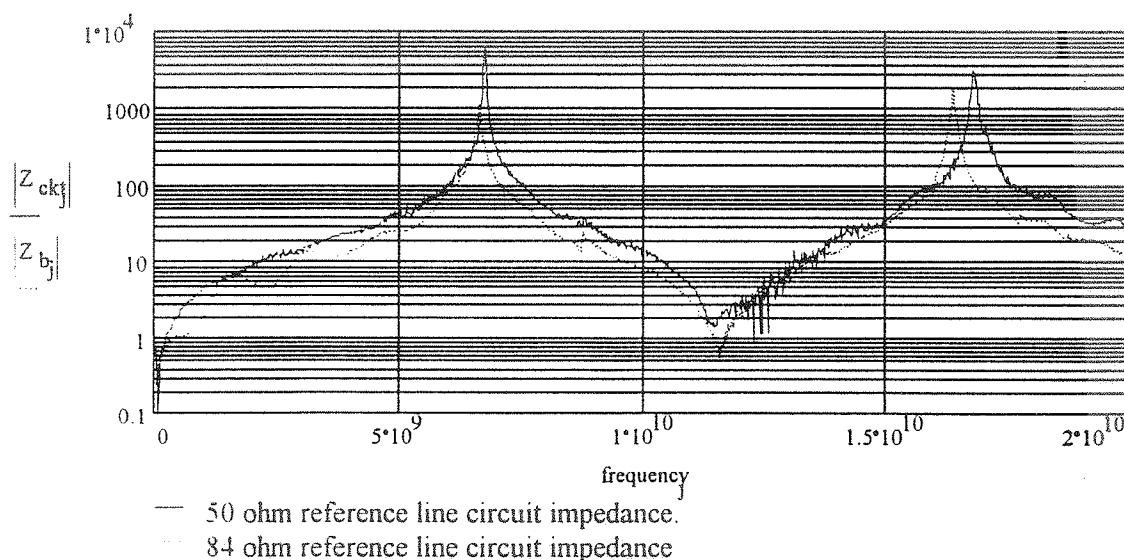


Figure 5-26. Measured circuit impedances (Ω) from the S_{21} measurements versus frequency (Hz).

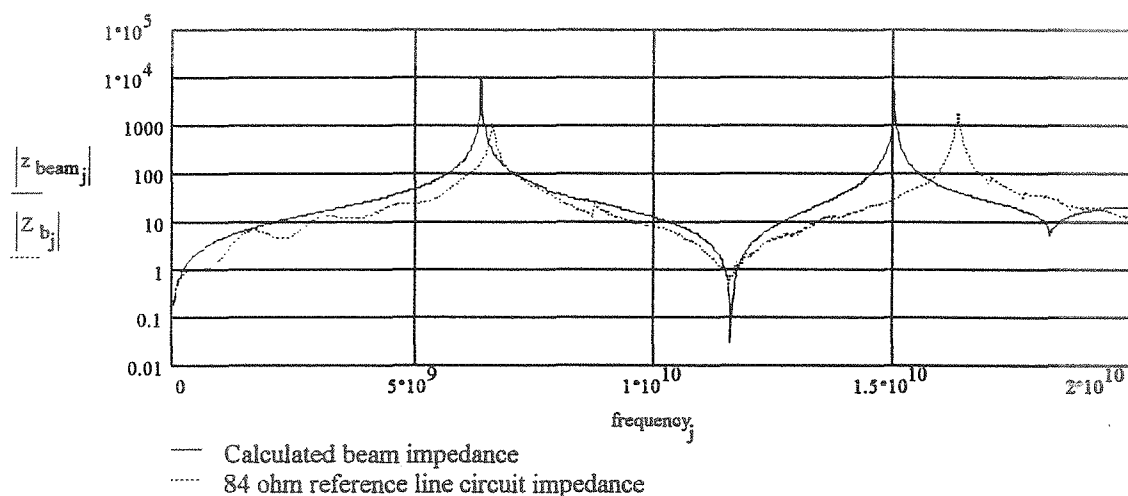


Figure 5-27. Plot of predicted beam impedance (Ω) with the measured circuit impedance (Ω) using an 84- Ω reference line versus frequency (Hz).

frequencies. The 84- Ω line, however, did not accurately measure the magnitude of the beam impedance at the cavity resonance. At the cavity resonance, the 84- Ω line was off by one order of magnitude from the 50- Ω measurement. The 50- Ω line measured the magnitude of the beam impedance accurately but shifted the resonant frequencies.

D. Conclusion

Stretched wire measurements are a complicated measurement and great care must be exercised when using this technique. Because of the TEM loss mechanism, the computations to solve Eq. 1-12 are generally easier for the center conductor problem in order to find the scattered waves from the pillbox cavity. In practice care must be used to align the center conductor in order to *not* excite high-order

ϕ -dependent cavity modes.

Use of both 50- Ω and high-wave impedance reference lines is necessary. At resonance, the lower wave impedance line may accurately measure the magnitude of the beam impedance but has an inherent error in its center frequency because of the presence of the center conductor. The high impedance line accurately measures the resonant frequency of cavity modes but is off in the magnitude of the impedance.

The SWM is a measurement of a linear system. Many network analyzers have band limitations of ~20-26.5 GHz. Time-domain measurements, while noisy, may be accurately made and may increase the bandwidth of the SWM.

VI. Summary and Conclusions

The design of a stable accelerator requires an understanding of the interaction between a charged bunch and its environment. The longitudinal beam impedance is a measure of the electric field, caused by an ultra-relativistic impulse of charge, along the trajectory of the ultra-relativistic charge. This interaction between an ultra-relativistic charge and its environment produces electromagnetic fields which are defined as the wakefield. The presence of the wakefield is a particular problem faced by accelerator scientists. By design, the interaction of charged particle beams with their environment is both constructive and destructive to the operation of accelerators.

Wakefield accelerator machines have been built which directly measure the beam impedance. These machines have several inherent problems. They are very expensive and, for a variety of reasons, measurements on these machines are costly. The machines are not portable and have very specific geometry requirements for a general DUT. Finally, wakefield accelerator measurements inherently have low signal-to-noise ratios. High noise levels often require a change in the DUT to achieve an appropriate signal-to-noise ratio.

The SWM was proposed as a method to estimate the beam impedance. The SWM requires the use of a commercially

available network analyzer or pulsing network. Stretched wire measurements are performed by first placing a wire upon the designed trajectory of a charged particle bunch. After the wire is in place, an impulse of current is excited on the wire, and its network parameters are measured. The lumped circuit impedance measured by the network analyzer is hypothesized to be equal to the longitudinal beam impedance.

Clearly, the addition of a wire inside the beampipe changes the boundary conditions inside the accelerator. Placement of a wire along the trajectory of the charged particle bunch changes the boundary conditions of the system such that the wakefield at this position identically vanishes. The effectiveness of the SWM technique, however, relies upon energy storage in the discontinuity region of the beampipe.

The SWM technique was proposed as a simple measurement for finding the effects of the environment on charged particle beams. In this dissertation the SWM was shown to provide excellent results for frequencies where the field intensities are similar between the open beampipe and the boundary conditions dictated by the center conductor beampipe, i.e., $E_z(r \approx 0, z, \omega) \approx 0$. For frequencies where $E_z(r \approx 0, z, \omega) \approx 0$, the method of excitation, whether it is an impulse of current excited on a wire or an ultra-relativistic charged particle bunch, is irrelevant. The SWM is not,

however, a suitable technique to measure the beam impedance for frequencies where a strong electric field on axis exists in the open beampipe, i.e., $E_z(r \approx 0, z, \omega) \neq 0$. A rough estimate of the beam impedance may be found for these frequency regimes through manipulation of data from stretched wire measurements by use of both high-impedance and low-impedance reference lines.

The integral equation of Eq. 1-12 describes the solution to the electric and magnetic field distributions for the wire and charged particle beam excitations. Using the complex Fourier series analysis presented in this dissertation solves Eq. 1-12 and correctly estimates the measured beam and circuit impedances. This general use of complex Fourier series analysis allows one to find circuit models for different cavity and beampipe geometries.

When it is assumed that there are no losses in the system, i.e., perfectly conducting boundaries, the calculated data for the beam impedance has to be modified slightly for frequencies below the first cutoff frequency of the open beampipe. This modification technique was pointed out in Ch. IV.C.ii in Figs. 4-3 and 4-4. The adjustment was performed using a comparison to two simple coupling circuit models over a narrow bandwidth about the resonant frequency of the cavity. One circuit model had loss, whereas the other was lossless. The propagating modes of the beampipe add an

effective loss mechanism and for frequencies above the first cutoff frequency it is no longer necessary to modify the calculated beam impedance.

All of the cavity modes, both TM and TEM, were solved for in this analysis. A problem in the analysis of Gluckstern et al. was related to their not using TEM modes in the cavity region. It was shown in an example that the DC mode, or magneto-static mode of the cavity, allows the stretched wire measurement to converge to the beam impedance correctly.

Use of high-impedance wires to estimate the beam impedance may not necessarily always be the best choice for a SWM. Reflections in the matching network can become significant and even mask the measured circuit impedance. The high-impedance reference line does not disturb the cavity's resonant frequency significantly when compared with the resonant frequency measured with an open beampipe. A low-impedance reference line, on the other hand, profoundly changes the resonant frequency. The coupling to the cavity modes is disturbed by the size of the wire, and the value of the measured circuit impedance may not converge to the actual beam impedance.

It was shown in Ch. V that the stretched wire measurement is a linear measurement. This implies that either frequency-domain measurements or time-domain

measurements may be made to obtain similar results. Frequency-domain measurements with network analyzers may possess high signal-to-noise ratios and have a broad dynamic range. Additionally, frequency-domain measurements are generally easier and more repeatable. On the other hand, pulse forming networks are significantly cheaper than network analyzers. Therefore, when cost is an issue, time-domain measurements are the best alternative.

Ease of application, cost, and discovery of spurious problems make the SWM an essential technique for measuring the beam impedance. These spurious problems include discontinuities in beampipes or possibly poor connectors at the beampipe-cavity interface. The existence of these problems requires that great care be exercised in the interpretation of stretched wire measurements.

Investigation of three-dimensional, non- ϕ symmetric sources should provide interesting theoretical, numerical, and measurement results for both the longitudinal and transverse impedance phenomena.

Appendix A

Derivation of Relationship Between Beam Impedance and Wakefield

Consider an ultra-relativistic particle of charge Q traveling through space confined to a straight line (for the moment, assume that this direction is the Cartesian unit vector \hat{z}). The charge Q encounters a wakefield electric field $\vec{E}(\vec{r}, t) = E_z(\vec{r}, t) \hat{z}$ caused by another ultra-relativistic particle of charge \tilde{q} , which is exactly t_f seconds ahead of the charge Q . This electric field caused by the charge \tilde{q} does work on the particle Q :

$$W(t_f) = -Q \int_{-\infty}^{\infty} E_z(r=0, z=c(\tau - t_f), \tau) dz.$$

A change of coordinates $z=ct$ shows

$$W(t_f) = -Qc \int_{-\infty}^{\infty} E_z(r=0, z=c(\tau - t_f), \tau) d\tau.$$

The beam impedance is defined to be the Fourier transformed wakefunction $w(t)$

$$Z(\omega) = \mathcal{F}\{w(t)\}.$$

The wakefunction is a scaled function of the wake-work function $W(t)$

$$w(t) = \frac{W(t)}{Q\tilde{q}}.$$

The beam impedance is therefore

$$Z(\omega) = \mathcal{F} \left\{ \frac{W(t_f)}{Q\tilde{q}} \right\} = -\frac{c}{\tilde{q}} \int_{-\infty}^{\infty} e^{-i\omega t_f} dt_f \int_{-\infty}^{\infty} E_z(r=0, z=c(\tau-t_f), \tau) d\tau.$$

Switching the order of integration and making the substitution that

$$z=c(\tau-t_f) \quad dz=-cdt_f$$

produces the result

$$\begin{aligned} Z(\omega) &= -\frac{1}{\tilde{q}} \int_{-\infty}^{\infty} d\tau \int_{-\infty}^{\infty} E_z(r=0, z, \tau) e^{-i\omega(-\frac{z}{c}+\tau)} dz \\ &= -\frac{1}{\tilde{q}} \int_{-\infty}^{\infty} d\tau \int_{-\infty}^{\infty} E_z(r=0, z, \tau) e^{ikz} e^{-i\omega\tau} dz. \end{aligned}$$

Finally, switching the order of integration one last time and rearranging terms reveals

$$= -\frac{1}{\tilde{Q}} \int_{-\infty}^{\infty} e^{ikz} dz \int_{-\infty}^{\infty} E_z(r=0, z, \tau) e^{-i\omega\tau} d\tau.$$

The second integration is simply the Fourier transform with respect to time of the electric field. The final equation is

$$Z(\omega) = -\frac{1}{\tilde{Q}} \int_{-\infty}^{\infty} E_z(r=0, z, \omega) e^{ikz} dz. \quad (\text{A-1})$$

Appendix B

Fourier Transform Definitions and Conventions

The Fourier transform pair used throughout this dissertation is

$$A(\omega) = \mathcal{F}\{a(t)\}_t = \int_{-\infty}^{\infty} a(t) e^{-i\omega t} dt$$

and

$$a(t) = \mathcal{F}^{-1}\{A(\omega)\}_\omega = \frac{1}{2\pi} \int_{-\infty}^{\infty} A(\omega) e^{i\omega t} d\omega.$$

Both the spatial Fourier transform and the time Fourier transform are used throughout this dissertation. To distinguish between these operations, let ω be the frequency variable for Fourier transforms with respect to the time variable, and let q be the frequency variable for Fourier transforms with respect to the space variable z . The transformed variable in functions is shown subscripted.

Appendix C

Fourier Transform Property

We want to determine the Fourier transform of $\int_{-\infty}^{\infty} f(z') h(z+z') dz'$. Using the definition of the Fourier transform in Appendix B, a short derivation follows.

Starting with

$$\mathcal{F} \left\{ \int_{-\infty}^{\infty} f(z') h(z+z') dz' \right\}_z = \int_{-\infty}^{\infty} e^{-iqz} dz \int_{-\infty}^{\infty} f(z') h(z+z') dz',$$

first interchange the order of integration:

$$= \int_{-\infty}^{\infty} f(z') dz' \int_{-\infty}^{\infty} e^{-iqz} h(z+z') dz. \quad (\text{C-1})$$

Using the definition of a shifted Fourier transformed signal,

$$\mathcal{F} \{x(z-z_o)\}_z = e^{-iqz_o} X(q)$$

shows that the right-hand integral of Eq. C-1 is

$$= H(q) \int_{-\infty}^{\infty} dz' f(z') e^{iqz'}.$$

Examination of the integral reduces this to the final result

$$\mathcal{F} \left\{ \int_{-\infty}^{\infty} f(z') h(z+z') dz' \right\}_z = H(q) F(-q).$$

Appendix D

Beampipe and Cavity Matrix Element Computations

A. Primary Integration Result

The following list of integrals is used frequently throughout the theoretical and numerical analysis. Asymptotics of these expressions are used to estimate the truncation error.

The following two integrals are used in calculating the elements of the pipe matrix:

$$\int_0^g dy \int_0^g dx e^{i \frac{2n\pi x}{g}} e^{-ik|x-y|} e^{-i \frac{2m\pi y}{g}} = \frac{2(1-e^{-ikg}) \left(k^2 + \frac{4\pi^2 mn}{g^2} \right)}{\left(k^2 - \left[\frac{2m\pi}{g} \right]^2 \right) \left(k^2 - \left[\frac{2n\pi}{g} \right]^2 \right)} \quad m \neq n$$

$$= \frac{-2igk \left(k^2 - \left[\frac{2n\pi}{g} \right]^2 \right) + 2(1-e^{-ikg}) \left(k^2 + \frac{4\pi^2 n^2}{g^2} \right)}{\left(k^2 - \left[\frac{2n\pi}{g} \right]^2 \right)^2} \quad m = n$$

B. Explicit Formulae for the Pipe and Cavity Matrices

Using the previous two integrals and the definitions for the pipe kernel given in Eqs. 1-6 and 1-8, the off-diagonal ($l \neq p$) elements of Θ are:

$$\theta_{l,p} = \frac{4\pi i}{a} \sum_{s=1}^{\infty} \frac{\left(1 - e^{-i\frac{b_s g}{a}}\right) \left(\left(\frac{b_s g}{a}\right)^2 + \frac{4\pi^2 l p}{g^2}\right)}{\left(\left(\frac{b_s g}{a}\right)^2 - \left(\frac{2l\pi}{g}\right)^2\right) \left(\left(\frac{b_s g}{a}\right)^2 - \left(\frac{2p\pi}{g}\right)^2\right)} \quad (D-1)$$

$$\frac{4\pi i}{a} \sum_{s=0}^{\infty} \frac{\alpha_s \left(1 - e^{-i\frac{\tilde{b}_s g}{a}}\right) \left(\left(\frac{\tilde{b}_s g}{a}\right)^2 + \frac{4\pi^2 l p}{g^2}\right)}{\left(\left(\frac{\tilde{b}_s g}{a}\right)^2 - \left(\frac{2l\pi}{g}\right)^2\right) \left(\left(\frac{\tilde{b}_s g}{a}\right)^2 - \left(\frac{2p\pi}{g}\right)^2\right)}$$

The diagonal (l=p) elements are:

$$\theta_{p,p} = \frac{4\pi i}{a} \sum_{s=1}^{\infty} \frac{\left(1 - e^{-i\frac{b_s g}{a}}\right) \left(\left(\frac{b_s g}{a}\right)^2 + \frac{4\pi^2 p^2}{g^2}\right) - i \frac{b_s g}{a} \left(\left(\frac{b_s g}{a}\right)^2 - \left(\frac{2p\pi}{g}\right)^2\right)}{\left(\left(\frac{b_s g}{a}\right)^2 - \left(\frac{2p\pi}{g}\right)^2\right)^2} \quad (D-2)$$

$$\frac{4\pi i}{a} \sum_{s=0}^{\infty} \frac{\alpha_s \left(1 - e^{-i\frac{\tilde{b}_s g}{a}}\right) \left(\left(\frac{\tilde{b}_s g}{a}\right)^2 + \frac{4\pi^2 p^2}{g^2}\right) - i \frac{\tilde{b}_s g}{a} \left(\left(\frac{\tilde{b}_s g}{a}\right)^2 - \left(\frac{2p\pi}{g}\right)^2\right)}{\left(\left(\frac{\tilde{b}_s g}{a}\right)^2 - \left(\frac{2p\pi}{g}\right)^2\right)^2}$$

The following three integrals are used to calculate the elements of the cavity matrix:

$$\int_0^g dy \int_0^g dx e^{i\frac{2m\pi x}{g}} \cos\left(\frac{n\pi y}{g}\right) \cos\left(\frac{n\pi x}{g}\right) e^{-i\frac{2p\pi y}{g}}$$

$$= \frac{16g^2 m p}{\pi^2 (n^2 - 4m^2) (n^2 - 4p^2)}$$

n odd

$$g^2$$

$$n=m=p=0$$

$$\frac{g^2}{4}$$

$$2n=|m|=|p|\neq 0$$

The cavity matrix is defined by using these expressions and applying the definition of the cavity kernel. Each element of the cavity matrix is defined by a sum of like terms from both the TM and TEM modes, which will be presented accordingly. Before presenting the TM components of $\underline{\underline{\mathbf{E}}}$, make the following two definitions:

$$P(\beta_m, r) = Y_1(\beta_m r) J_0(\beta_m b) - J_1(\beta_m r) Y_0(\beta_m b),$$

$$A_m = \frac{P^2(\beta_m, a)}{b^2 P^2(\beta_m, b) - a^2 P^2(\beta_m, a)}.$$

The first contribution is a result of TM modes and adds to every element of the $\underline{\underline{\mathbf{E}}}$ matrix:

$$\xi_{TM\,l,p} = \sum_{n=0}^{\infty} \sum_{m=1}^{\infty} \left[\frac{\frac{128glp}{\pi} A_m}{k^2 - \beta_m^2 - \left(\frac{(2n+1)\pi}{g} \right)^2} \right] \frac{1}{((2n+1)^2 - 4l^2) ((2n+1)^2 - 4p^2)} \cdot (D-3)$$

The next contribution, a result of TM modes, adds only to the diagonal and anti-diagonal ($l=p$, $l=-p$) elements of $\underline{\underline{\Xi}}$:

$$\xi_{\pm p, \pm p} = \pi g (1 + \delta_{p,0}) \delta_{|l|, |p|} \sum_{m=0}^{\infty} \frac{A_m}{\left[k^2 - \beta_m^2 - \left(\frac{2p\pi}{g} \right)^2 \right]}. \quad (\text{D-4})$$

The next contribution to the cavity matrix comes from the TEM modes; it contributes to every element of $\underline{\underline{\Xi}}$:

$$\xi_{l,p} = \sum_{n=0}^{\infty} \frac{\frac{-64g^3 lp}{a^2 \pi^3 \ln(\frac{b}{a})}}{\left((2n+1)^2 - 4p^2 \right) \left((2n+1)^2 - 4l^2 \right) \left((2n+1)^2 - \left(\frac{kg}{\pi} \right)^2 \right)}. \quad (\text{D-5})$$

The final TEM contribution to the cavity matrix adds only to the diagonal and anti-diagonal elements:

$$\xi_{\pm p, \pm p} = \frac{\pi g}{a^2 \pi^3 \ln(\frac{b}{a})} \frac{(1 + \delta_{p,0}) \delta_{|l|, |p|}}{k^2 - \left(\frac{2p\pi}{g} \right)^2}. \quad (\text{D-6})$$

C. Truncation Error Analysis

Truncation errors in the pipe and cavity matrices will introduce error in the analysis. The truncation errors were

estimated by converting the truncated infinite summations of Eqs. D-1, D-2, D-3, D-4, and D-5 into an integration. This technique required several assumptions regarding the point of truncation for each of the series based on the geometry of Fig 1-9. The following integrals are used to estimate the truncation errors. Assume that $a^2, b^2,$ and c^2 are purely real quantities. Further assumptions are listed by the individual integrals:

$$\int \frac{dx}{x^2+a^2} = \frac{1}{a} \tan^{-1}\left(\frac{x}{a}\right) \quad a^2 > 0$$

$$\int \frac{dx}{x^2-a^2} = \frac{1}{2a} \ln\left(\frac{x-a}{x+a}\right) \quad a^2 > 0$$

$$\int \frac{dx}{x(x^2-a^2)} = -\frac{1}{2a^2} \ln\left(\frac{x^2}{x^2-a^2}\right) \quad a^2 \neq 0$$

$$\int \frac{dx}{x^3(x^2-a^2)} = -\frac{1}{2a^4} \ln\left(\frac{x^2}{x^2-a^2}\right) + \frac{1}{2a^2 x^2} \quad a^2 \neq 0$$

$$\int \frac{dx}{x^2(x^2-a^2)^2} = -\frac{3}{4a^5} \ln\left(\frac{x-a}{x+a}\right) - \frac{x}{2a^4(x^2-a^2)} - \frac{1}{a^4 x} \quad a^2 > 0$$

$$\int \frac{dx}{x^3 (x^2 - a^2)^2} = \frac{1}{a^6} \ln \left(\frac{x^2}{x^2 - a^2} \right) - \frac{1}{2a^4 x^2} - \frac{1}{2a^4 (x^2 - a^2)} \quad a^2 \neq 0$$

$$\int \frac{dx}{(x^2 + a^2)^2} = \frac{1}{2a^3} \tan^{-1} \left(\frac{x}{a} \right) + \frac{x}{2a^2 (x^2 + a^2)} \quad a^2 > 0$$

$$\int \frac{dx}{(x^2 - a^2)^2} = -\frac{1}{4a^3} \ln \left(\frac{x-a}{x+a} \right) - \frac{x}{2a^2 (x^2 - a^2)} \quad a^2 > 0$$

$$\int \frac{x^2 dx}{(x^2 + a^2)^2} = \frac{1}{2a} \tan^{-1} \left(\frac{x}{a} \right) - \frac{x}{2(x^2 + a^2)} \quad a^2 > 0$$

$$\int \frac{x^2 dx}{(x^2 - a^2)^2} = \frac{1}{4a} \ln \left(\frac{x-a}{x+a} \right) - \frac{x}{2(x^2 - a^2)} \quad a^2 > 0$$

$$\int \frac{x dx}{(x^2 - a^2)^2} = -\frac{1}{2(x^2 - a^2)} \quad a^2 \neq 0$$

$$\int \frac{dx}{x(x^2 - a^2)^2} = \frac{1}{2a^4} \ln \left(\frac{x^2}{x^2 - a^2} \right) - \frac{1}{2a^2 (x^2 - a^2)} \quad a^2 \neq 0$$

$$\int \frac{dx}{(x^2 + a^2)(x^2 + b^2)} = \frac{1}{b(a^2 - b^2)} \tan^{-1} \left(\frac{x}{b} \right) + \frac{1}{a(b^2 - a^2)} \tan^{-1} \left(\frac{x}{a} \right) \quad \begin{matrix} a^2, b^2 > 0 \\ a^2 \neq b^2 \end{matrix}$$

$$\int \frac{x^2 dx}{(x^2 + a^2)(x^2 + b^2)} = \frac{a \tan^{-1} \left(\frac{x}{a} \right) - b \tan^{-1} \left(\frac{x}{b} \right)}{a^2 - b^2} \quad \begin{matrix} a^2, b^2 > 0 \\ a^2 \neq b^2 \end{matrix}$$

$$\int \frac{dx}{x(x^2+a^2)(x^2+b^2)}$$

$$a^2 \neq b^2 \\ a^2 \neq 0, b^2 \neq 0$$

$$= \frac{1}{2b^2(a^2-b^2)} \ln\left(\frac{x^2}{x^2-b^2}\right) + \frac{1}{2a^2(b^2-a^2)} \ln\left(\frac{x^2}{x^2-a^2}\right)$$

$$\int \frac{dx}{(x^2-a^2)(x^2-b^2)^2}$$

$$a^2 \neq b^2 \\ a^2, b^2 > 0$$

$$= \frac{\ln\left(\frac{x-a}{x+a}\right)}{2a(a^2-b^2)^2} + \frac{(a^2-3b^2)\ln\left(\frac{x-a}{x+a}\right)}{4b^3(b^2-a^2)^2} - \frac{x}{2b^2(b^2-a^2)(x^2-b^2)}$$

$$\int \frac{dx}{x^2(x^2-a^2)(x^2-b^2)}$$

$$a^2 \neq b^2 \\ a^2, b^2 > 0$$

$$= -\frac{1}{a^2b^2x} + \frac{\ln\left(\frac{x-a}{x+a}\right)}{2a^3(a^2-b^2)} + \frac{\ln\left(\frac{x-b}{x+b}\right)}{2b^3(b^2-a^2)}$$

$$\int \frac{dx}{x^3(x^2-a^2)(x^2-b^2)}$$

$$a^2 \neq b^2 \\ a^2 \neq 0, b^2 \neq 0$$

$$= -\frac{1}{2a^2b^2x^2} + \frac{a^4\ln\left(\frac{x^2}{x^2-b^2}\right) - b^4\ln\left(\frac{x^2}{x^2-a^2}\right)}{2a^4b^4(a^2-b^2)}$$

$$\int \frac{dx}{(x^2-a^2)(x^2-b^2)(x^2-c^2)}$$

$$\begin{array}{l} a^2 \neq b^2 \neq c^2 \\ a^2, b^2, c^2 > 0 \end{array}$$

$$= \frac{\ln\left(\frac{x-a}{x+a}\right)}{2a(a^2-b^2)(a^2-c^2)} + \frac{\ln\left(\frac{x-b}{x+b}\right)}{2b(b^2-a^2)(b^2-c^2)} + \frac{\ln\left(\frac{x-c}{x+c}\right)}{2c(c^2-a^2)(c^2-b^2)}$$

Appendix E

Derivation of Circuit Parameters from S_{21} Measurements

A. *Introduction*

It is desired to find the circuit impedance embedded in the scattering parameters measured with a network analyzer. While the procedure for finding the impedance from the transmission coefficient is only presented, the procedure for using the reflection coefficient follows in the same manner. In the laboratory it is common to use the transmission instead of reflection for practical requirements. The reference sections used in stretched wire measurements are designed to have low reflection. The relative error in the measurement of the reflected energy therefore is higher than the relative error in the measurement of transmission. The transmission coefficient is specifically analyzed to find the circuit impedance in this dissertation since the reflected energy is, by design, very small. Theoretically, use of either transmission or reflection coefficients to find the lumped impedance will produce identical results.

B. *Background Theory*

Imagine the circuit depicted in Fig. E-1, a lumped impedance Z with two transmission lines connected to it of characteristic impedance R_0 . From transmission line theory, the voltage and current in region I is

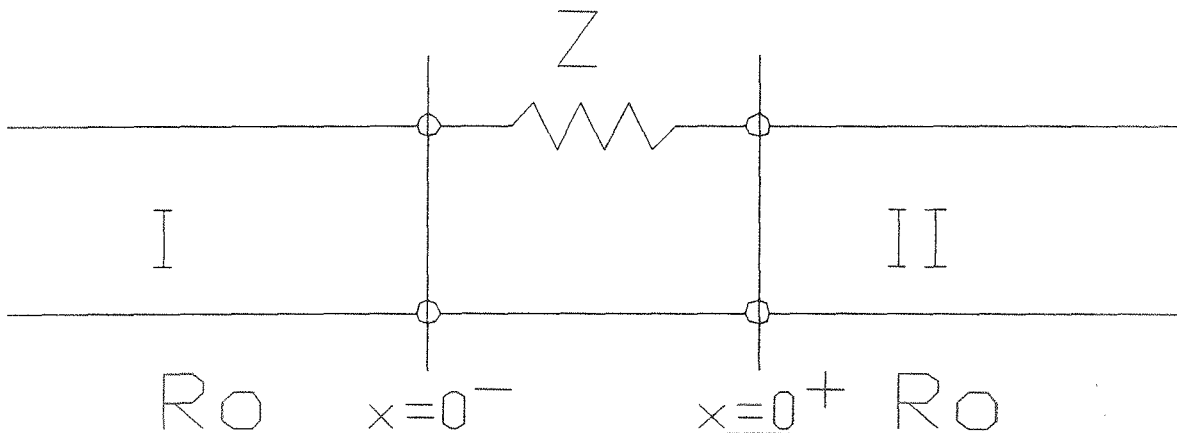


Figure E-1. Lumped impedance Z with two transmission lines of characteristic impedance R_o connected.

$$V(x) = V^+ e^{-i\beta x} + V^- e^{i\beta x} \quad I(x) = \frac{1}{R_o} (V^+ e^{-i\beta x} - V^- e^{i\beta x})$$

and the voltage and current in region II is

$$V(x) = \tilde{V}^+ e^{-i\beta x} \quad I(x) = \frac{1}{R_o} \tilde{V}^+ e^{-i\beta x}.$$

The boundary conditions demand that the current into the impedance is identical to the current out of the impedance:

$$I|_{x=0^-} = I|_{x=0^+}.$$

This produces a relationship that

$$V^+ - V^- = \tilde{V}^+.$$

The voltage drop from region I to II divided by the impedance Z is another expression for the current through the impedance Z . Applying the rule of continuity of current reveals the relationship

$$\frac{V^+ + V^- - \tilde{V}^+}{Z} = \frac{1}{R_o} \tilde{V}^+. \quad \text{E-2}$$

Inserting Eq. E-1 into E-2 reveals the relationship

$$\frac{\tilde{V}^+}{V^+} = S_{21} = \frac{2R_o}{Z + 2R_o}.$$

Rearranging this equation shows the dependence of Z on S_{21} :

$$Z = \frac{2R_o(1 - S_{21})}{S_{21}}. \quad \text{E-3}$$

C. Application of Background Theory to SWM

Stretched wire measurements usually require two separate measurements. The first measurement is of the reference line; the second is of the reference line with the DUT. Assume that the impedance mismatches of the reference line are independent of the particular DUT. This implies that

$$Z_{DUT} = Z_{ref+DUT} - Z_{ref}.$$

Inserting this relationship into Eq. E-3 reveals

$$Z_{DUT} = \frac{2R_o(1-s_{21DUT+ref})}{s_{21DUT+ref}} - \frac{2R_o(1-s_{21ref})}{s_{21ref}}.$$

Rearranging this equation produces

$$Z_{DUT} = \frac{2R_o(s_{21ref} - s_{21DUT+ref})}{s_{21DUT+ref}s_{21ref}}.$$

This equation is used throughout Ch. V for finding the measured circuit impedance of the pillbox cavity.

Appendix F

Bibliography

- [1] A. Oppenheim, A. Willsky, and I. Young, "Signals and Systems," Prentice-Hall, pp. 69-250, 1983.
- [2] E. Ginzton, "Microwave Measurements," McGraw-Hill, pp. 391-434.
- [3] M. Sands, J. Rees, SLAC-report PEP-95, August 1974.
- [4] H. Henke, "Point Charge Passing a Resonator with Beam Tubes," CERN-report CERN-LEP-RF/85-41, November 1985.
- [5] R. L. Gluckstern, "High-frequency behavior of the Longitudinal Impedance for a Cavity of General Shape," Physical Review D, Volume 39 Number 9, pp. 2773-2779, 1 May 1989.
- [6] R. Li, R. L. Gluckstern, "The Analytical and Numerical Investigation of the Longitudinal Coupling Impedance," Ph.D. Thesis, University of Maryland, 1990.
- [7] S. A. Heifets, S. A. Kheifets "Coupling Impedance in Modern Accelerators," SLAC-PUB-5297, September 1990.
- [8] D. A. Edwards and M.J. Syphers, "An Introduction to the Physics of High Energy Accelerators," John Wiley & Sons, pp. 186-189, 1993.
- [9] Teichmann and Wigner, J. Appl. Phy., April, 1953.
- [10] G. M. Wing, "A Primer on Integral Equations of the First Kind," Society for Industrial and Applied Mathematics, Series Issue No. 27, November 1991.
- [11] H. Henke, private communication.
- [12] C. Deibele, R. Kustom, J. Beyer, private communication.
- [13] J. Simpson, P. Schoessow, A. Ruggiero, J. Norem, R. Konecny, W. Gai, H. Figueroa, "Direct Measurement of Beam-Induced Fields in Accelerating Structures," ANL/HEP/PR/88/04 WF-78.
- [14] C. Deibele, R. Kustom, J. Beyer, private communication.
- [15] P. Guidée, H. Hahn, Y. Mizumachi, "The Longitudinal

Coupling Impedance of a Double-Step Cross Section
Change in the Vacuum Chamber," BNL 50829, March 1978.

- [16] M. Abramowitz, I. A. Stegun, "Handbook of Mathematical Functions," Dover, pp. 358-362, 1972.
- [17] F. Caspers, "Bench Methods for Beam Coupling Impedance Measurements," Proceedings of the Coupling Impedance Measurements Techniques Workshop, Argonne National Laboratory, Advanced Photon Source, 8/12/91.
- [18] J. Gubner, private communication.